

Optical Characterization of Interface Magnetization in Multifunctional Oxide
Heterostructures

Fan Fang

Wuhu, Anhui, P. R. China

Bachelor of Science, University of Science and Technology of China, 2009

A Dissertation presented to the Graduate Faculty
of the College of William and Mary in Candidacy for the Degree of
Doctor of Philosophy

Department of Applied Science

The College of William and Mary
May, 2016

APPROVAL PAGE

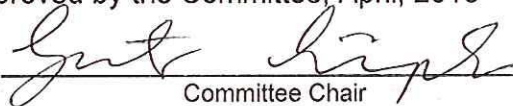
This Dissertation is submitted in partial fulfillment of
the requirements for the degree of

Doctor of Philosophy



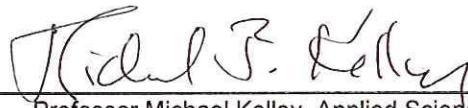
Fan Fang

Approved by the Committee, April, 2016



Committee Chair

Professor Gunter Luepke, Applied Science
The College of William and Mary



Professor Michael Kelley, Applied Science
The College of William and Mary



Professor Mark Hinders, Applied Science
The College of William and Mary



Prof. Qi Li, Physics
Pennsylvania State University

ABSTRACT

Multifunctional oxides attract much attention recently. The strong correlated electron system involves the notable properties of colossal magnetoresistance, ferroelectric tunneling and spin transport, with the coupling of electron, spin and orbital degrees of freedom. Their rich functional behavior is of potential use for nanoelectronics and data storage. Particularly interesting are the multiferroic materials, which exhibit simultaneously electric and magnetic ordering properties. Understanding the interface coupling mechanism of these two order parameters are critical to future development of high-performance spintronic devices. The goal of this dissertation is to elucidate the interfacial magnetoelectric (ME) coupling with optical characterization method -- magnetization-induced second-harmonic generation (MSHG), which is sensitive to the interface due to the broken spatial inversion symmetry.

First, ME coupling at the interface of BaTiO_3 (BTO)/ $\text{La}_{0.67}\text{Sr}_{0.33}\text{MnO}_3$ (LSMO) is observed by applying an external electric field. The voltage-dependent magnetic contrast reveals a sharp transition from ferromagnetic (FM) to antiferromagnetic (AFM) order occurring at positive voltage (applied to LSMO contact). This novel effect is attributed to interface ME coupling. Strain or ferroelectric (FE) polarization induced mechanisms do not play an important role in this system. A new mechanism is proposed -- minority spin injection -- to modulate the interface magnetization. The minority spin injection at the interface weakens the double-exchange coupling of nearby e_g electrons, thereby weakening the FM ordering. Thus the dominant AFM superexchange coupling of localized t_{2g} electrons causes the phase transition at positive voltage. The magnetic transition is shifted to higher voltage by reducing the carrier concentration of BTO.

Second, a non-multiferroic heterostructure -- SrTiO_3 (STO)/ $\text{La}_{0.5}\text{Ca}_{0.5}\text{MnO}_3$ (LCMO)/ $\text{La}_{0.67}\text{Sr}_{0.33}\text{MnO}_3$ (LSMO) -- is studied to elucidate further the interface ME effect. The magnetization transition is observed but shifted to negative voltage. The LSMO is pushed to higher hole doping level due to the STO layer which acts as a hole donating layer, while the LCMO interlayer at the medium doping level displays complicated CE-type AFM phase. Thus, a negative voltage is required to lower the hole doping level of LSMO to induce the FM phase. The magnetic contrast reappears at high positive voltage, indicating the occurrence of an A-type AFM phase, which is stable at high hole doping concentration. The results of this dissertation show that the interface magnetic phase of LSMO can be controlled by an applied electric field through modulation of the hole doping level.

TABLE OF CONTENTS

| | |
|--|-----|
| Acknowledgements | iv |
| Dedications | v |
| List of Tables | vi |
| List of Figures | vii |
| Chapter 1. Introduction | 1 |
| 1.1 Magnetic tunneling junction | 1 |
| 1.2 Spin transfer torque | 3 |
| 1.3 Magnetoelectric effect | 5 |
| 1.3.1 Magnetoelectric effects on ferromagnetic metal | 6 |
| 1.3.2 Magnetoelectric effect in multiferroic oxide heterostructures | 6 |
| 1.3.3 Magnetoelectric effect in spin transport | 8 |
| 1.4 Scope of dissertation | 9 |
| Chapter 2. Experimental Techniques | 12 |
| 2.1 Magneto-optic Kerr effect | 12 |
| 2.2 Magnetization-induced second-harmonic-generation | 16 |
| 2.2.1 Second-harmonic generation | 16 |
| 2.2.2 Nonlinear magnetic susceptibility | 17 |
| 2.3 Experimental setup | 20 |
| 2.3.1 The ultrafast laser system | 20 |
| 2.3.2 MOKE and MSHG experimental setup | 23 |

| | |
|---|----|
| Chapter 3. Magnetolectric coupling in $\text{BaTiO}_3/\text{La}_{0.67}\text{Sr}_{0.33}\text{MnO}_3$ | |
| heterostructure | 25 |
| 3.1 Introduction | 25 |
| 3.1.1 Motivation | 26 |
| 3.1.2 Basic properties of $\text{La}_{1-x}\text{Sr}_x\text{MnO}_3$ | 27 |
| 3.1.3 Basic properties of BaTiO_3 | 31 |
| 3.2 Samples and experiments | 32 |
| 3.2.1 Sample preparation and characterization | 32 |
| 3.2.2 MSHG and MOKE experiments | 34 |
| 3.3 Results | 36 |
| 3.3.1 Interfacial magnetic transition induced by magnetolectric effect | 36 |
| 3.3.2 Voltage-dependent second-harmonic generation | 39 |
| 3.3.3 Effect of $\text{La}_{0.5}\text{Ca}_{0.5}\text{MnO}_3$ interlayer | 41 |
| 3.3.4 Effect of dopants in BaTiO_3 layer | 46 |
| 3.4 Discussion | 49 |
| 3.4.1 Possible mechanisms for interfacial magnetolectric effect | 49 |
| 3.4.2 Microscopic mechanism for interfacial magnetolectric effect | 56 |
| Chapter 4. Magnetolectric coupling in $\text{SrTiO}_3/\text{La}_{0.5}\text{Ca}_{0.5}\text{MnO}_3/\text{La}_{0.67}\text{Sr}_{0.33}\text{MnO}_3$ heterostructure | 58 |

| | |
|--|----|
| 4.1 Introduction | 58 |
| 4.1.1 Basic properties of SrTiO_3 | 58 |
| 4.1.2 Basic properties of $\text{La}_{1-x}\text{Ca}_x\text{MnO}_3$ | 59 |
| 4.2 Samples and experiments | 62 |
| 4.3 Results and discussion | 63 |
| 4.3.1 Interfacial magnetic transition induced by magnetoelectric effect | 63 |
| 4.3.2 Effects of dopants in SrTiO_3 | 67 |
| Chapter 5. Summary | 72 |
| Bibliography | 75 |

ACKNOWLEDGEMENTS

I am truly grateful to everyone who have directly or indirectly supported me during the completion of the work. First and Foremost, I wish to express my appreciation to Professor Gunter Luepke for his guidance and mentoring throughout my doctoral study at the College of William and Mary. He has always provided enthusiasm and perspective for the research process, and this work would not be possible without his support and guidance.

I am particularly grateful to Professor Qi Li and her group member: Yuewei Yin. Thank you for their discussion about the multiferroic materials. I am indebted to them for providing a series of high-quality manganites samples and the characterization work. I also appreciate to their fruitful scientific discussion about the projects.

I also thank my lab mates: Haowei Zhai, Xin Ma, Wei Zheng, Yichun Fan, Xiao Liu, Peiwen Liu. I appreciate their friendship and collective encouragement to finish this dissertation. In particular, I am thankful to Haowei Zhai for assistance in data collection and discussion. I have enjoyed every moment that we worked together.

I express my appreciation to my doctoral dissertation defense committee members: Professor Michael Kelley of Applied Science, Professor Mark Hinders of Applied Science and Professor Qi Li of Physics (Pennsylvania State University). Thank you for their participation, comments and suggestion in the review of this dissertation.

Finally, I wish to express my sincere gratitude to my family: Yuqi Fang, Jindi Cheng. Their truly and constant love and encouragement have always been the source of my strength and motivation. In particular, I appreciate my girl friend Xiaji Liu for her understanding and great support during my doctoral study.

This dissertation is dedicated to my family

LIST OF TABLES

- 2.1 The Fresnel coefficients for p -polarized light incident on the magnetic layer system with dielectric constant of ϵ . θ_1 and θ_2 denote the incident and refracted angle in the magnetic layer. The substitution $\alpha_1 = \cos \theta_1$ and $\alpha_2 = \cos \theta_2$ are used. The Voigt coefficients Q_P , Q_L and Q_T are the polar, longitudinal and transverse projection of the Voigt vector \vec{Q} , respectively, which are proportional to the magnitude of the magnetization components along the corresponding directions.

15

LIST OF FIGURES

| | | |
|-----|--|----|
| 1.1 | Schematic spin tunneling process in MTJ | 2 |
| 1.2 | Principle of MRAM in the "cross point" architecture | 3 |
| 1.3 | Schematic of writing into MRAM cell with STT effect | 5 |
| 2.1 | Geometry of longitudinal, transverse, and polar Kerr effects | 14 |
| 2.2 | MSHG hysteresis loop measured with the sample LSMO/LCMO/STO. Red dash lines are two magnetization stages. | 20 |
| 2.3 | Sketch of the setup to measure the pulse duration | 21 |
| 2.4 | Schematic setup of compressor in the "RegA 9000" laser system. CM1, CM2, CM3 are compressor optics. DG is the diffraction grating. The position micrometer allows adjustment of the grating along the mount's horizontal axis. | 22 |
| 2.5 | Pulse duration adjusted by a) position micrometer (four different marked positions) and b) rotation screw (three rotations). Pulse duration is compressed and the pulse energy is increased with sharper peak. c) Pulse duration determined with sech^2 fitting for rotation 2. | 23 |
| 2.6 | Sketch of the MOKE & MSHG setup | 24 |
| 3.1 | Perovskite structure of compounds with chemical formula $R_xA_{1-x}MO_3$ | 26 |
| 3.2 | Schematic representation of the crystal-field splitting of the 3d orbital of Mn ion. a) corresponds to the cubic, while b) corresponds to the tetragonal configuration with lattice spacing c (between the layers) larger than a and b (in plane of the layer). | 28 |

| | | |
|------|---|----|
| 3.3 | Phase diagram of LSMO as concentration of Sr, courtesy of Y. Tokura and Y. Tomioka, prepared with data from reference 86 and 93. PM, PI, FM, FI and CI denote paramagnetic metal, paramagnetic insulator, FM metal, FM insulator, and spin-canted insulator states, respectively. T_C is the Curie temperature and T_N is the Néel temperature. | 29 |
| 3.4 | Idealized density of states $N(E)$ for a half-metallic ferromagnetic. The Fermi energy is in the middle of a spin up band, but in between bands for the spin down band. | 30 |
| 3.5 | Illustration of the changes of BTO transforms from a paraelectric cubic into ferroelectric tetragonal phase with temperature. The permittivity curve represents data measured on a BTO ceramic. The arrows show possible directions of the spontaneous polarization. The unit cell is represented by a square in the cubic phase and rectangle in the tetragonal phase. | 32 |
| 3.6 | Ferroelectric polarization hysteresis loop of BTO from oxygen poor BTO/LSMO sample | 33 |
| 3.7 | Cross-sectional annular dark-field STEM image at the interface region of LSMO/BTO/LCMO/LSMO tunnel junction. The inset is the low-loss (EELS) map representing spectroscopic signatures of LSMO (blue), BTO (red) and LCMO (green) | 34 |
| 3.8 | Schematic of the optical measurements. MOKE measures the bulk magnetization of the LSMO film, while MSHG selectively probes the interface magnetization only. LSMO and ITO are two electrodes where a voltage is applied. | 35 |
| 3.9 | I-V curve of oxygen poor BTO/LSMO sample at 80 K. Inset is the semi-log current curve. | 35 |
| 3.10 | Schematic band diagram of the n-type Schottky contact. E_C , E_V , E_F and V_{bi} denote conduction band, valence band, Fermi level and build-in potential, respectively. | 36 |

| | |
|---|----|
| 3.11 MSHG hysteresis loops at different voltage | 37 |
| 3.12 Magnetic contrast A determined from MSHG measurements as a function of gate voltage U_g | 38 |
| 3.13 MOKE hysteresis loops at different voltage | 39 |
| 3.14 Magnetic contrast A determined from MOKE measurements as a function of gate voltage U_g | 39 |
| 3.15 a) $P_{in}P_{out}$ SHG signal measured at 80 K and the inset shows a comparison between the square-rooted $P_{in}P_{out}$ SHG curve (labeled in black and red) and the P-V loop (labeled in violet). b) $S_{in}S'_{out}$ SHG signal measured at 80 K | 41 |
| 3.16 I-V curve of oxygen-poor BTO/LCMO/LSMO sample. Inset represents I-V curve on log scale | 42 |
| 3.17 Hysteresis loops with different voltage applied | 42 |
| 3.18 Magnetic contrast as a function of gate voltage U_g | 42 |
| 3.19 a) $P_{in}P_{out}$ SHG signal and b) $S_{in}S'_{out}$ signal as a function of gate voltage U_g | 43 |
| 3.20 a) MOKE hysteresis loop of BTO/LCMO at 80K and b) Comparison of coercivities between MOKE and MSHG of BTO/LCMO/LSMO at 80 K | 44 |
| 3.21 a) MSHG and b) MOKE hysteresis loops with different voltage applied | 45 |
| 3.22 Magnetic contrast as a function of gate voltage U_g . | 45 |
| 3.23 a) I-V curve, inset is semi-log curve. b) P-V curve | 47 |
| 3.24 a) C-V curve; b) Carrier concentration calculated from C-V measurement | 47 |
| 3.25 MSHG hysteresis loops at a series of voltage | 48 |

| | |
|--|----|
| 3.26 MSHG magnetic contrast as a function of gate voltage U_g | 48 |
| 3.27 $S_{in}S'_{out}$ SHG as a function of gate voltage U_g | 48 |
| 3.28 Capacitance as a function of gate Voltage U_g | 52 |
| 3.29 Concentration of oxygen poor sample | 53 |
| 3.30 Linear fitting to determine the build-in potential | 54 |
| 3.31 Schematic model of spin alignment at BTO/LSMO interface. a) Below critical gate voltage U_c , majority spins (red arrows) of Mn^{3+} and Mn^{4+} ions are double-exchange coupled (right panel), leading to a ferromagnetic state of LSMO. b) Above U_c , The AFM super-exchange interaction of t_{2g} electrons between neighboring Mn ions dominates, and the interfacial LSMO layer undergoes a FM-to-AFM phase transition. | 55 |
| 3.32 Schematic band diagram of the n-type BTO/LSMO Schottky junction for $U_g > U_c$, depicting the electron current J , ferroelectric polarization P , and considering an AFM-ordered LSMO interface layer and a half-metallic LSMO electrode with only spin-up states at the Fermi level E_F . | 57 |
| 4.1 Phase diagram of $La_{1-x}Ca_xMnO_3$, obtained using magnetization and resistivity data, reproduced from S.-W. Cheong and H. Y. Hwang. FM: ferromagnetic Metal, FI: Ferromagnetic Insulator, AF: Antiferromagnetism, CAF: Canted Antiferromagnetism and CO: Charge/Orbital Ordering. | 61 |
| 4.2 a) C-type unite cell and b) E-type unit cell. c) The spin structure in plane at $x = 1/2$. Open can solid circle denote the spin up and down electrons, respectively. The white and gray squares denote the C- and E- type unit cells, respectively. At $x = 1/2$, C-type and E-type unit cells are equal. The thick blue and red lines indicate the zigzag FM path. | 61 |

| | | |
|------|---|----|
| 4.3 | Current-Voltage (I-V) curve shows diode effect. Inset is the semi-log curve | 63 |
| 4.4 | MSHG hysteresis loops at different voltage | 64 |
| 4.5 | Magnetic contrast A determined from MSHG measurements as a function of gate voltage U_g | 64 |
| 4.6 | MOKE hysteresis loops at different voltage | 66 |
| 4.7 | MOKE contrast A as a function of gate voltage U_g | 66 |
| 4.8 | a) $P_{in}P_{out}$ and b) $S_{in}S'_{out}$ SHG measured at 80K | 67 |
| 4.9 | Current-Voltage (I-V) curve shows diode effect. Inset is the semi-log curve. | 69 |
| 4.10 | MSHG hysteresis loops at different voltage | 69 |
| 4.11 | MSHG magnetic contrast A as a function of gate voltage U_g | 70 |
| 4.12 | MOKE hysteresis loops at different voltage | 70 |
| 4.13 | a) $P_{in}P_{out}$ and b) $S_{in}S'_{out}$ SHG measured at 80K | 71 |

Chapter 1

Introduction

Electrons have charge and spin, which have been considered separately until recently. In traditional electronic devices, electrical charges are moved by an electric field to transport information and are stored in a capacitor to save it. Increasing the integration density of electronic devices leads to faster processing speed due to the shorter distance of the electron transport. However, the following challenge emerges: the heat generated by the charging and discharging process causes a high temperature, which can ruin the function of a transistor as the integration density increases.

The spintronics technology offers the opportunity to solve the problem. It is not based on the conduction by electrons or holes as in semiconductor devices but relies on the different transport properties of the majority spin and minority spin electrons.

1.1 Magnetic tunneling junction

The discovery in 1988 of giant magneto-resistance (GMR) on Fe/Cr magnetic multilayers¹ is considered the beginning of the new spin-based electronics. The resistance is lowest when the magnetic moments in ferromagnetic (FM) layers are aligned parallel and highest when aligned anti-parallel. The GMR ratio is defined as:

$$GMR = (R^{AP} - R^P) / R^P , \quad (1.1)$$

where R^P and R^{AP} are the resistances in the parallel and antiparallel state, respectively. The GMR ratio can be 80% at helium temperature and 20% at room temperature.

By replacing the non-magnetic metallic spacer layer by a thin non-magnetic insulating layer, higher magnetoresistance can be achieved, thus creating a magnetic tunnel junction (MTJ). In this configuration, the electrons travel from one FM layer to the other by a tunneling effect, which conserves the spin (Fig. 1.1)². The first MTJs used an amorphous Al_2O_3 insulating layer that can reach a tunneling magneto-resistance (TMR) ratio of around 70% at room temperature³. Much higher effects were observed with the MgO barrier^{4,5}. The MgO barrier is active in selecting a symmetry of high spin polarization, leading to the record values of 1010% at 5K, and 500% at room temperature⁶.

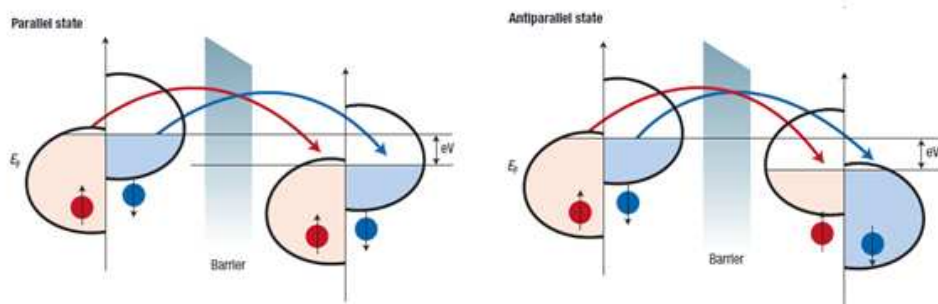


Fig. 1.1 Schematic spin tunneling process in MTJ^[2]

MTJ's have been widely used in read-heads of hard-drive disks and magnetic sensors. In addition, researchers have started to develop the magnetic random access memory (MRAM)⁷. Figure 1.2 shows the principle of MRAM in the "cross-point" architecture². The binary information 0 and 1 is recorded on the two opposite orientations of the magnetization of the free layer along the easy axis.

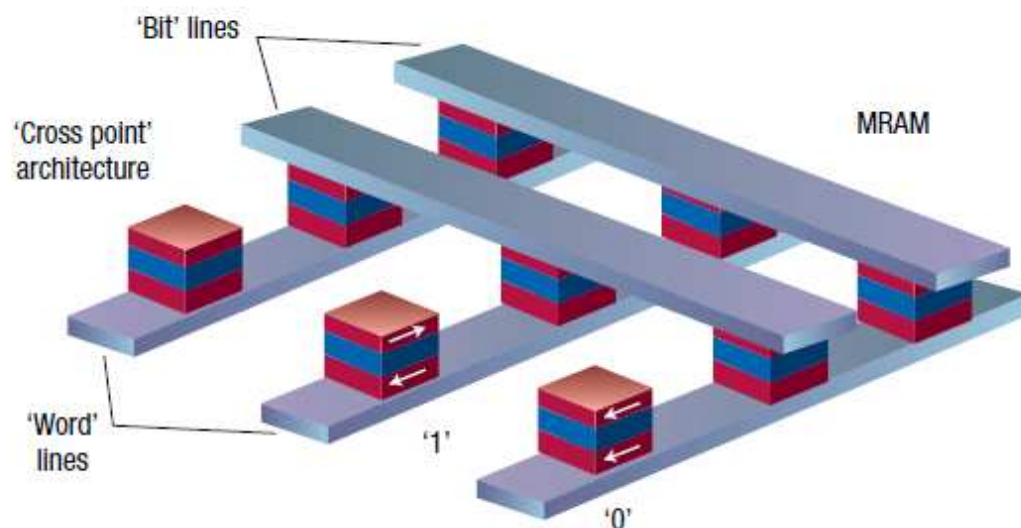


Fig. 1.2 Principle of MRAM in the "cross point" architecture ^[2]

1.2 Spin transfer torque

The use of a magnetic field to write the information is still considered a limitation. The information is stored in the form of magnetization orientation of a nanoparticle of volume. By reducing the volume, we need to increase the writing field to overcome the thermal excitations. However, the power available

to create it decreases as the dimensions are downscaled.

Spin-transfer torque (STT) provides a new route for writing magnetic information. The magnetization orientation of a free magnetic layer can be controlled by direct transfer of spin-angular momentum from a spin-polarized current. The first experimental demonstration of the low and high magnetoresistance states by STT effect is carried out with a Co/Cu/Co multilayer system in 2000⁸. The polarized current flows through the FM layer with different magnetization orientation. The *s-d* exchange coupling results in a torque tending to align the magnetization of the layer towards the spin moment of the incoming electrons. The amplitude of the torque per unit area is proportional to the injected current density, so that the writing current decreases proportionally to the cross-sectional area.

The principle of writing into MRAM cell with STT effect is shown in Fig 1.3². Electrons flow from the thick FM layer F_1 with certain magnetization orientation to the thin free FM layer F_2 , and the magnetization of F_2 would be favored parallel to that of F_1 with STT effect. When the electrons flow from the thin free layer F_2 to F_1 , a strong spin scattering process occurs at the thick layer. The back-scattered electrons with antiparallel spin orientation apply a torque in the thin layer to switch it antiparallel to that of F_1 . The dynamical behavior is studied through a modified Landau-Lifshitz-Gilbert equation describing the damped precession of magnetization with the effect of STT and thermal excitation⁹.

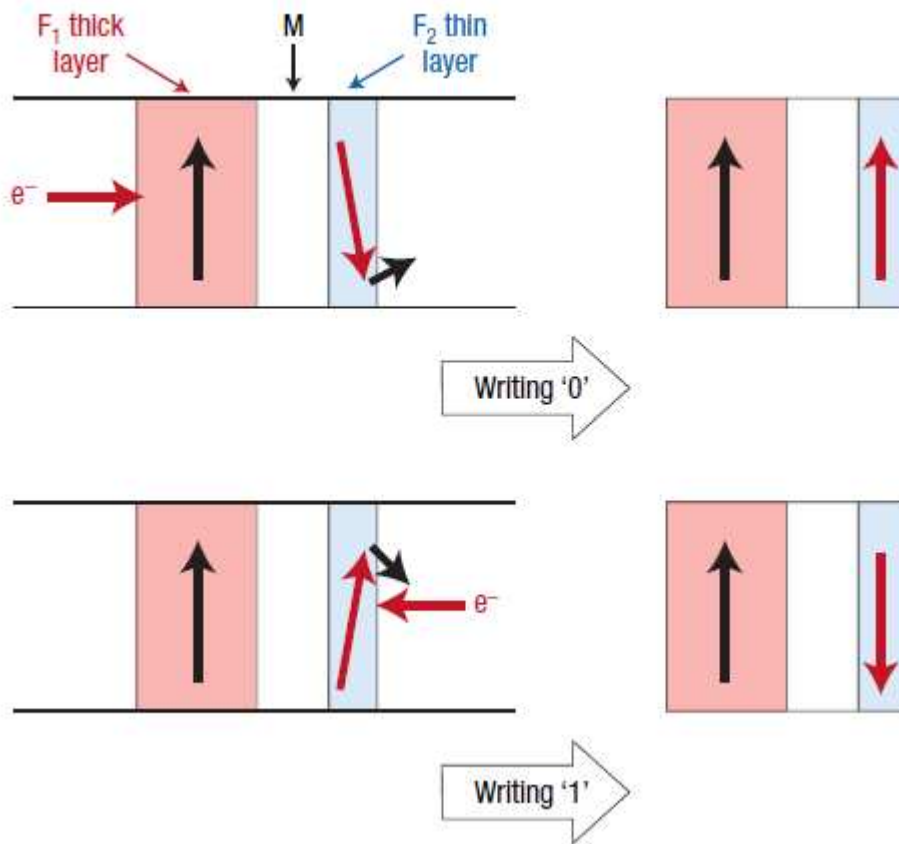


Fig. 1.3 Schematic of writing into MRAM cell with STT effect. ^[2]

1.3 Magnetoelectric effect

The switching of the magnetic state is accomplished by applying a current. The large current density required leads to significant energy loss from heating. Generating an electric field with integrated devices is more convenient and energy-favorable. Controlling magnetism by electric fields via magnetoelectric (ME) materials has recently attracted significant interest with the approaching scaling and power consumption limits.

1.3.1 Magnetoelectric effects on ferromagnetic metal

When a metal surface is exposed to an electric field, the induced surface charge screens the electric field over a characteristic screening length of the metal. In a FM metal, the screening charge is spin-dependent due to the exchange splitting of the spin majority and spin minority density of states (DOS)¹⁰. As a result, the surface magnetization changes with electric field. The magnitude of the effect depends on the Fermi-level spin polarization of the surface DOS, increasing with larger polarization up to the maximum 100 percent spin-polarized materials: half-metals¹¹. The ME effect can be further enhanced by using a ferroelectric (FE) material to form FM/FE interface. The polarization charges at the interface in response to the electric field enhance the spin-dependent screening.

In addition to the screening mechanism, the interface bonding change during polarization reversal also plays an important role in ME effect at the FM/FE interface¹². Orbital hybridizations are altered with the change in atomic displacement to affect the interface magnetic moments.

1.3.2 Magnetoelectric effect in multiferroic oxide heterostructures

Transition metal oxides (TMOs) are ideal candidates for the study of ME coupling, as the strongly correlated d electrons constrained at a given lattice site induce a local entanglement of the charge, spin and orbital degrees of freedom¹³. The competition between different interactions in such strongly

correlated electron systems results in a complex phase diagram, which builds a platform to manipulate the coupling between those order parameters. For example, the magnetic superexchange interaction could be adjusted by the polar bond-bending distortion between Mn and O ions in $\text{Sr}_{1/2}\text{Ba}_{1/2}\text{MnO}_3$, which causes large negative ME coupling¹⁴; ME coupling strength could also be modulated by controlling the strain state (lattice order)¹⁵, Dzyaloshinskii-Moriya interaction^{16,17}, and Jahn-Teller distortion¹⁸. Despite of the profound physics in such TMO systems, the obtained ME coupling in the bulk of complex multiferroic oxides is weak^{19–21}. The hopes of achieving practical devices based on single-phase materials have been renewed recently by the discovery of room-temperature ME effects in ferromagnetic multicomponent TMOs, such as $\text{Sr}_3\text{Co}_2\text{Fe}_{24}\text{O}_{41}$ ²², $\text{Sr}_3\text{Co}_2\text{Ti}_2\text{Fe}_8\text{O}_{19}$ ²³, Aurivillius-phase oxides^{21,24}, $[\text{Pb}(\text{Zr}_{0.53}\text{Ti}_{0.47})\text{O}_3]_{0.6}-[\text{Pb}(\text{Fe}_{0.5}\text{Ta}_{0.5})\text{O}_3]_{0.4}$ solid solutions^{25,26}, and epitaxial $\epsilon\text{-Fe}_2\text{O}_3$ ²⁷, $\text{Ga}_{1-x}\text{Fe}_{1+x}\text{O}_3$ ²⁸, and LuFeO_3 ²⁹ thin films.

An alternative but challenging approach is the ME coupling across interfaces of multifunctional oxide heterostructures consisting of a FE and a FM component^{13,30–32}, which could be amplified by a “bridge” between them, such as FE/antiferromagnetic (AFM)/FM coupling in $\text{BiFeO}_3/\text{La}_{1-x}\text{Sr}_x\text{MO}_3$ system^{33,34}, strain state^{30,35,36}, and charge transfer processes^{37,38}. As a result, some progress has been achieved in these multifunctional heterostructures with the relative strong ME coupling at room temperature, like the magnetization reversal triggered by an electric field³⁹. The interfaces of TMO

heterostructures offer a unique and important experimental test-bed as spatial symmetry is broken by the structure itself, and different phases could be combined at the atomic-level^{40–43}. Also, two-dimensionality usually enhances the effects of electron correlations by reducing their kinetic energy. Considering these features of oxide interfaces, many novel effects and functions that cannot be attained in the bulk form might appear. As a result, different symmetry constraints can be used to design structures exhibiting phenomena not found in the bulk constituents. For example, at the domain walls and structural interfaces, the emergent behavior with properties that deviate significantly from the bulk appears in BiFeO_3 ⁴⁴ and ErMnO_3 ⁴⁵. Indeed, theory has predicted the possibility of significant changes in the interfacial magnetization and spin polarization in a ferromagnet in response to the ferroelectric polarization state across the interface^{11,12,37,46}.

1.3.3 Magnetoelectric effect in spin transport

Electrical modulation of conductivity in multiferroic tunnel junctions (MFTJs), in the configuration of a FE thin-film layer as the tunnel barrier sandwiched between two ferromagnetic layers, has received significant attention^{47–50}. The key property is the tunnel electroresistance (TER) effect. Polarization affects the interface transmission function by changing the electrostatic potential at the interface, the interface bonding strength, and strain associated with the piezoelectric response⁵⁰. In the MFTJ, the TER and

tunnel magnetoresistance (TMR) effects coexist, making MFTJ a four-stage resistance device where resistance can be switched by both electric and magnetic fields. Recently, MFTJs consisting of BaTiO₃ tunnel barriers and La_{0.7}Sr_{0.3}MnO₃ electrodes exhibit a TER of up to 10,000% by inserting a nanometer-thick La_{0.5}Ca_{0.5}MnO₃ interlayer⁴⁹.

1.4 Scope of dissertation

A fundamental understanding of the interface ME effect in multiferroic oxide heterostructures is the major focus of this dissertation. Although the interfacial ME behavior is to some extent studied by correlated electron and spin transportation through the interface in magnetic tunneling junctions (MTJs)^{51–53}, direct characterization of interfacial spin states is still missing. The resolution of most techniques to investigate magnetic states like SQUID can only reach several nanometers, which is already way beyond the thickness of the interface. Some others with higher surface sensitivity, such as high-resolution transmission electron microscopy, require sample pretreatment by ion milling or mechanical polishing which may cause an artificial effect on the interface properties^{54–57}. In contrast, optical second-harmonic generation (SHG) is a convenient tool to study magnetic and charge states at buried interfaces^{58–60}, and it thus turns out to be suitable for investigating interfacial ME coupling. In centrosymmetric materials, such as TMOs with perovskite structure, SHG is allowed only at surfaces and interfaces that break the

inversion symmetry. Hence without modifying the sample, buried interfaces are accessible by the SHG technique provided that they lie within the penetration depth of light (~ 100 nm).

Chapter 2 introduces some basic experimental techniques to characterize optically the bulk and interface properties. Magnetization-induced second-harmonic generation (MSHG) is a nonlinear optical effect, which is interface sensitive to selectively probe the interface magnetization. Magneto-optic Kerr effect (MOKE) is used to probe the bulk property. The experimental setup is also described.

Chapter 3 presents the ME coupling at the interface of the multiferroic heterostructure BaTiO_3 (BTO)/ $\text{La}_{0.67}\text{Sr}_{0.33}\text{MnO}_3$ (LSMO). By applying an external electric field, an interface FM-AFM transition is observed at positive voltage (applied to LSMO layer), which is attributed to ME coupling. Strain and FE polarization mediated mechanisms are discussed, but they do not play an important role for the observed effect. A new mechanism is proposed -- minority spin injection -- to modulate the interface magnetization. In brief, the AFM superexchange interaction is strengthened and FM double-exchange coupling is weakened with the injection of minority spins. Moreover, a high voltage shift of the magnetic transition is observed by reducing the electron carrier concentration of BTO.

Chapter 4 presents the study of a non-multiferroic heterostructure system -- SrTiO_3 (STO)/ $\text{La}_{0.5}\text{Ca}_{0.5}\text{MnO}_3$ (LCMO)/ $\text{La}_{0.67}\text{Sr}_{0.33}\text{MnO}_3$ (LSMO) by replacing

the FE layer. The magnetization transition by ME coupling is also observed but at negative voltage, in contrast to BTO/LSMO heterostructure. The STO layer acts as a hole donating layer, and thus a negative voltage is required to lower the hole doping level of LSMO and to stabilize the FM phase at the interface. Moreover, an interface A-type AFM phase is also detected at high positive voltage, i.e. high hole concentration in LSMO. The results of this dissertation show that the interface magnetic phase of LSMO can be controlled by an applied electric field through modulation of the hole doping level.

Chapter 5 provides the summary of this dissertation.

Chapter 2

Experimental Techniques

This chapter presents the optical characterization techniques which have been widely used to study the magnetic properties of magnetic materials. Section 2.1 introduces the magneto-optic Kerr effect (MOKE) and optical geometries to measure the magnetization. Section 2.2 gives a basic introduction to the surface- and interface-sensitive probing technique -- magnetization-induced second-harmonic generation (MSHG). The experimental setup is described in section 2.3.

2.1 Magneto-optic Kerr effect

The magneto-optic Kerr effect was discovered by the Rev. John Kerr in 1877 when he was examining the polarization of the reflected light from the polished electromagnet pole. This effect can be observed as the change in the intensity and/or polarization state of the light reflected from a magnetic medium. Magneto-optics is presently described in the context of either microscopic quantum theory or macroscopic dielectric theory^{61,62}.

Microscopically, the effect originates from the spin-orbit coupling between the electrical field of the light and the electron spin, which gives rise to the large Faraday rotation in the ferromagnetic materials with the imbalanced population of spin-up and spin-down electrons. The electron seems as if it

moves through the electric field $-\nabla V$ with momentum \vec{p} inside a medium with spin-orbit coupling: $(\nabla V \times \vec{p}) \cdot \vec{s}$, which connects the magnetic and optical properties of a ferromagnet.

Macroscopic description of the magneto-optic effect is based on the dielectric properties of the magnetic medium, represented by the dielectric tensor⁶²:

$$\vec{\epsilon} = \epsilon \begin{bmatrix} 1 & iQ_z & -iQ_y \\ -iQ_z & 1 & iQ_x \\ iQ_y & -iQ_x & 1 \end{bmatrix}. \quad (2.1)$$

The linear polarized light can be expressed as the superposition of two circular polarized components, and the Faraday effect is the result of the propagating velocity difference between the two circular modes. From Maxwell's equation, the two normal modes propagating in the medium are left-circular polarized light with refraction index $n_L = n \left(1 - \frac{1}{2} \vec{Q} \cdot \hat{k}\right)$, and right-circular polarized light with refraction index $n_R = n \left(1 + \frac{1}{2} \vec{Q} \cdot \hat{k}\right)$, where $n = \sqrt{\epsilon}$ is the average refraction index, $\vec{Q} = (Q_x, Q_y, Q_z)$ is the Voigt vector, and \hat{k} is the unit vector along the direction of the light propagation. Thus, the Faraday rotation of the linear polarized light propagating through the medium with distance L is expressed as:

$$\theta = \frac{\pi L}{\lambda} (n_L - n_R) = -\frac{\pi L n}{\lambda} \vec{Q} \cdot \hat{k}, \quad (2.2)$$

where λ is the wavelength in the vacuum.

The difference between the real parts of n_L and n_R gives the phase shifts of the two normal modes, leading to a rotation of the polarization plane of

the light. Meanwhile, the difference between the imaginary part of n_L and n_R results in the different absorption rates for the two normal modes, affecting the ellipticity of the light.

The magneto-optic Kerr effect is categorized as three types according to the geometry of the magnetization in relation to the plane of the incidence and the plane of the sample: the longitudinal, transverse, and polar MOKE (Fig. 2.1). The longitudinal and transverse MOKE are observed at oblique angles of incidence with the difference of the applied magnetic field orientation relative to the optical plane of incidence. The applied field is parallel to the plane of the sample in these two geometries and is oriented parallel to the plane of incidence for longitudinal but perpendicular to the plane of the incidence in transverse condition. The polar MOKE is carried out with the applied field perpendicular to the sample surface, and often performed at normal incidence.

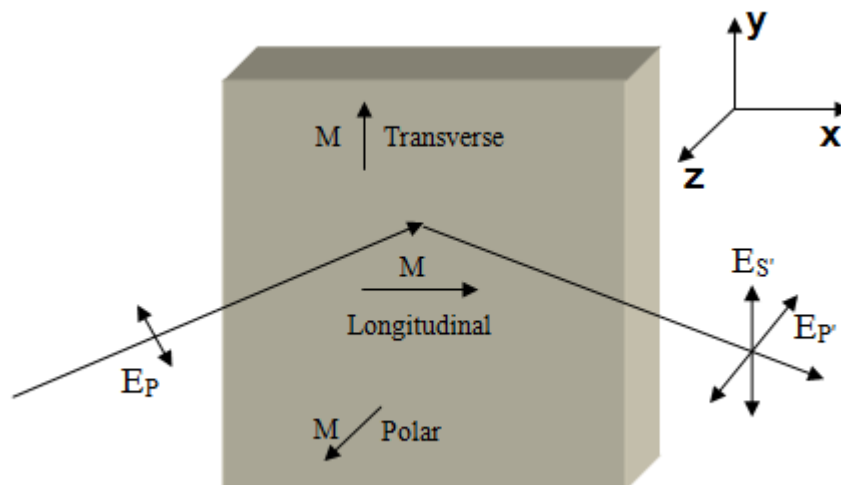


Fig. 2.1: Geometry of longitudinal, transverse, and polar Kerr effects.

The nature of the magneto-optic Kerr effect depends on the orientation of the magnetization with respect to the plane of incidence and the plane of the sample. In the longitudinal and polar conditions, the Kerr effect is shown as a change in the polarization state of the reflected light. However, the Kerr effect is seen as a change in the intensity of the reflected beam only (for p -polarized incident light), and no ellipticity occurs for transverse MOKE. This is summarized in Table 2.1^[63].

Table 2.1: The Fresnel coefficients for p -polarized light incident on the magnetic layer system with dielectric constant of ϵ . θ_1 and θ_2 denote the incident and refracted angle in the magnetic layer. The substitution $\alpha_1 = \cos \theta_1$ and $\alpha_2 = \cos \theta_2$ are used. The Voigt coefficients Q_P , Q_L and Q_T are the polar, longitudinal and transverse projection of the Voigt vector \vec{Q} , respectively, which are proportional to the magnitude of the magnetization components along the corresponding directions.^[63]

| | r_{pp} | r_{ps} |
|--------------|---|--|
| Polar | $\frac{\sqrt{\epsilon}\alpha_1 - \alpha_2}{\sqrt{\epsilon}\alpha_1 + \alpha_2}$ | $\frac{Q_p\sqrt{\epsilon}\alpha_1}{i(\sqrt{\epsilon}\alpha_1 + \alpha_2)(\alpha_1 + \sqrt{\epsilon}\alpha_2)}$ |
| Longitudinal | $\frac{\sqrt{\epsilon}\alpha_1 - \alpha_2}{\sqrt{\epsilon}\alpha_1 + \alpha_2}$ | $\frac{Q_L\sqrt{\epsilon}\alpha_1 \tan \theta_1}{i(\sqrt{\epsilon}\alpha_1 + \alpha_2)(\alpha_1 + \sqrt{\epsilon}\alpha_2)}$ |
| Transverse | $\frac{\sqrt{\epsilon}\alpha_1\sqrt{1 - Q_T^2/\alpha_2^2} - \alpha_2 - i\sqrt{\epsilon}Q_T\alpha_1 \tan \theta_2}{\sqrt{\epsilon}\alpha_1\sqrt{1 - Q_T^2/\alpha_2^2} + \alpha_2 - i\sqrt{\epsilon}Q_T\alpha_1 \tan \theta_2}$ | 0 |

Based on the Fresnel coefficients in Table 2.1, MOKE measurements are usually performed with linear p -polarized light incident to the sample and the s -component of the reflected beam is detected by the photodiode selected by the analyzer for longitudinal and polar measurements, while for the

transverse measurements, we detect the p -component of the reflected beam.

2.2 Magnetization-induced second-harmonic-generation

2.2.1 Second-harmonic generation

Second-harmonic generation (SHG) arises from the nonlinear polarization $P(2\omega)$ induced by the incident laser field $E(\omega)$. The polarization can be written as⁶⁴:

$$P(2\omega) = \chi^{(2)} E(\omega) E(\omega) + \chi^{(0)} E(\omega) \nabla E(\omega) + \dots \quad (2.3)$$

The lowest-order term in equation (2.3) describes an electric dipole source, where $\chi^{(2)}$ is a third-rank susceptibility tensor. Symmetry considerations show that this contribution is zero in a centrosymmetric medium, thus limiting electric dipole radiation to the interfaces where the inversion symmetry is broken. The second term in equation (2.3) describes the bulk second-harmonic generation with much smaller electric quadrupole-like contributions^{59,64}.

In the thin film condition, SHG is surface and interface sensitive, and can be described as:

$$P_i(2\omega) = \chi_{ijk}^{cr} E_j(\omega) E_k(\omega) \quad , \quad i, j, k = x, y, z \quad (2.4)$$

χ_{ijk}^{cr} is a third-rank susceptibility tensor with 27 elements describing the crystallographic contribution. For SHG, it is irrelevant in which order the incident electric field components appear, that is $E_j(\omega)$ and $E_k(\omega)$ are equivalent and can be exchanged, consequently the susceptibility is symmetric

in the last two indices: $\chi_{ijk}^{cr} = \chi_{ikj}^{cr}$. Then the susceptibility tensor can be reduced to 18 independent elements and can be expressed in the form of:

$$\begin{pmatrix} P_x \\ P_y \\ P_z \end{pmatrix} = \begin{pmatrix} \chi_{xxx} & \chi_{xyy} & \chi_{xzz} & \chi_{xxy} & \chi_{xyz} & \chi_{xzx} \\ \chi_{yxx} & \chi_{yyy} & \chi_{yzz} & \chi_{yyx} & \chi_{yyz} & \chi_{yzy} \\ \chi_{zxx} & \chi_{zyy} & \chi_{zzz} & \chi_{zxy} & \chi_{zyz} & \chi_{zzx} \end{pmatrix} \begin{pmatrix} E_x^2 \\ E_y^2 \\ E_z^2 \\ 2E_xE_y \\ 2E_yE_z \\ 2E_zE_x \end{pmatrix}. \quad (2.5)$$

The inversion symmetry is broken along the z-direction normal to the sample surface. With the symmetric operation $x \rightarrow -x$ (mirror reflection with y-z plane), we have $P_x \rightarrow -P_x$, $E_x \rightarrow -E_x$, while P_y and P_z keep constant. This will lead all the tensor components with odd number of index x to be zero. Similarly, we can get all the tensor components with odd number of index y to be zero under the symmetric operation $y \rightarrow -y$. Thus equation (2.5) can be written as:

$$\begin{pmatrix} P_x \\ P_y \\ P_z \end{pmatrix} = \begin{pmatrix} 0 & 0 & 0 & 0 & 0 & \chi_{xzz} \\ 0 & 0 & 0 & 0 & \chi_{yyz} & 0 \\ \chi_{zxx} & \chi_{zyy} & \chi_{zzz} & 0 & 0 & 0 \end{pmatrix} \begin{pmatrix} E_x^2 \\ E_y^2 \\ E_z^2 \\ 2E_xE_y \\ 2E_yE_z \\ 2E_zE_x \end{pmatrix}. \quad (2.6)$$

For the centrosymmetric system, all the components of the susceptibility tensor will reduce to zero, which means SHG is forbidden in this system.

2.2.2 Nonlinear magnetic susceptibility

The second-harmonic polarization of a magnetic medium is described by a third-rank nonlinear susceptibility tensor for the crystallographic contribution

χ_{ijk}^{cr} and a fourth-rank axial tensor χ_{ijkl}^m for the magnetization-induced part⁶⁵.

In the bulk of the centrosymmetric medium, the electric dipole contribution is forbidden. At the surface and interface, the inversion symmetry is broken, leading to the surface and interface induced components. The presence of a magnetization will not affect the inversion symmetry, but will introduce extra nonzero surface tensor elements to modify the nonlinear susceptibility, which will change sign when the orientation of the magnetization M is reversed. The surface and interface can be simplified to one third-rank tensor with even and odd components as:

$$P_i^{Mag}(2\omega) = \left(\chi_{ijk}^+(\pm M) \pm \chi_{ijk}^-(\pm M) \right) E_j(\omega) E_k(\omega) . \quad (2.7)$$

The odd component $\chi_{ijk}^-(\pm M)$ changes the sign with the magnetization reversal and therefore contributes to the magnetic asymmetry in the MSHG response.

The symmetry of the nonlinear susceptibility is determined by the symmetry of the particular surface under consideration. The nonzero elements of χ can be obtained under symmetry operations⁶⁶:

$$\chi_{ijk}(M_l) = \Sigma \Sigma \Sigma T_{ii'} T_{jj'} T_{kk'} \chi_{i'j'k'} . \quad (2.8)$$

where T is the transformation matrix for each symmetry operation. Take the longitudinal configuration for example, from the mirror operation in the y-z plane ($x \rightarrow -x$) with $P_x^{Mag} \rightarrow -P_x^{Mag}$, $E_x \rightarrow -E_x$ and P_y^{Mag} , P_z^{Mag} and M_x keeping constant, we can get all the components with odd number of index x are equal to zero. By applying the mirror operation in the x-z plane ($y \rightarrow -y$)

with $\mathbf{P}_y^{Mag} \rightarrow -\mathbf{P}_y^{Mag}$, $E_y \rightarrow -E_y$ and $\mathbf{M}_x \rightarrow -\mathbf{M}_x$, we can have the following result: the components with odd number of index y are not necessary to be zero and are odd to \mathbf{M}_x , while all other non-zero components are even to \mathbf{M}_x . In other words: χ_{xzx} , χ_{yyz} , χ_{zxx} , χ_{zyy} and χ_{zzz} are even components, while χ_{xyx} , χ_{yxx} , χ_{yyy} , χ_{yzz} and χ_{zyz} are odd components.

The MSHG response depends on the geometry of the magnetization in relation to the incident light and sample plane, similar to MOKE. The measured intensity in a certain experimental geometry can, in general, be written as a sum of effective tensor components:

$$I^{\pm}(2\omega) \propto |\chi_{eff}^{+}(2\omega) \pm \chi_{eff}^{-}(2\omega)|^2, \quad (2.9)$$

where χ_{eff}^{+} and χ_{eff}^{-} are linear combinations of the even and odd tensor elements and Fresnel factors:

$$\chi_{eff} = \Sigma \alpha_{ijk} \chi_{ijk}. \quad (2.10)$$

The magnetic contrast is defined as:

$$A = \frac{I(+M) - I(-M)}{I(+M) + I(-M)}, \quad (2.11)$$

where $I(+M)$ and $I(-M)$ are the MSHG signal intensities detected for the two magnetization states at positive or negative magnetic field (Fig. 2.2). The contrast is normalized to the total second-harmonic intensity and does not depend on the intensity of the fundamental light.

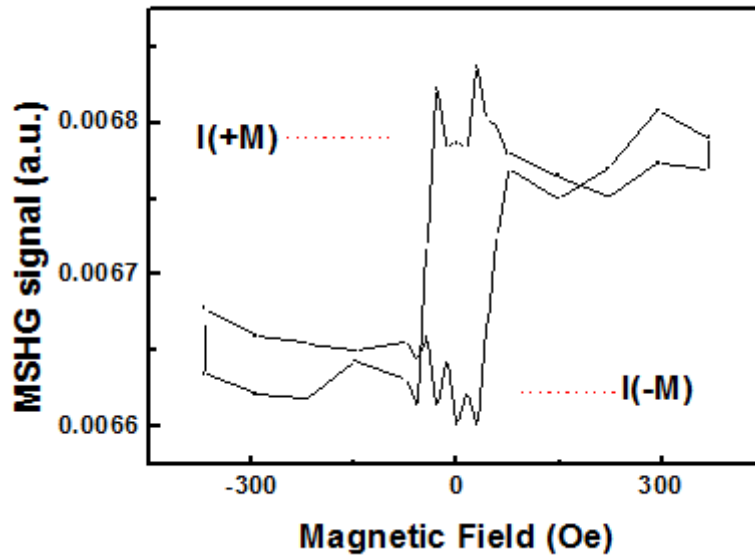


Fig. 2.2 MSHG hysteresis loop measured with the sample LSMO/LCMO/STO. Red dash lines are two magnetization stages.

2.3 Experimental setup

2.3.1 The ultrafast laser system

The experiments are performed with a femtosecond Ti:sapphire amplifier system. The 800-nm wavelength, mode-locked seed beam with 20-nm bandwidth generated from "Tsunami" is amplified by the "RegA 9000" system. The output is 200-femtosecond pulses with 4 μJ energy with the 250-kHz repetition at the 800-nm wavelength after compression. Pulse duration is one significant parameter related to the MSHG signal and is necessary to be optimized. The pulse duration can be measured by the "pump-probe" setup: the laser beam is split into two parts. One is modulated by the delay stage to

adjust the optical path difference of the two beams. Both of them are focused and finally overlapped spatially in the Beta-Barium-Borate Crystal (BBO), which is a nonlinear optical crystal with application of harmonics generation. A photodiode is used to detect the signal generated in the middle of the two beams through the BBO crystal, which represents the temporal overlap of the two beams (Fig. 2.3).

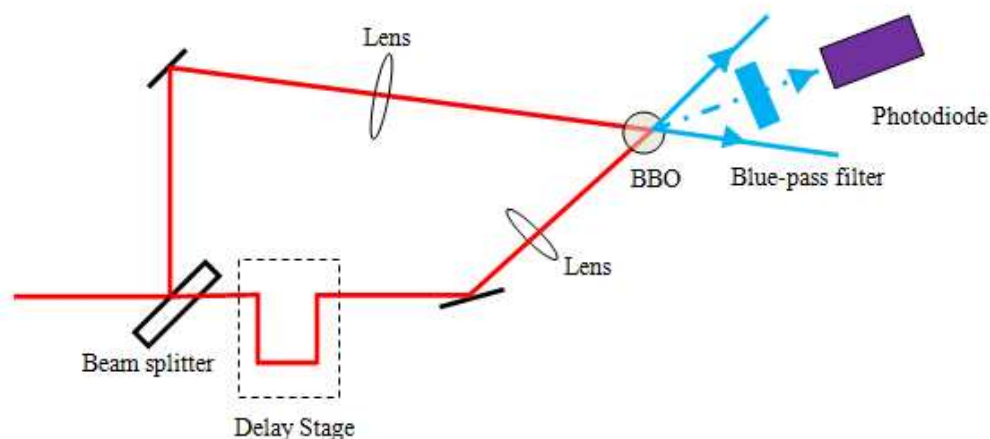


Fig. 2.3 Sketch of the setup to measure the pulse duration

The simplest way to compress the pulse width is to adjust the position micrometer and the rotation screw of the diffraction grating in the pulse compressor, as depicted in Fig. 2.4. The laser beam is compressed with four passes off the grating.

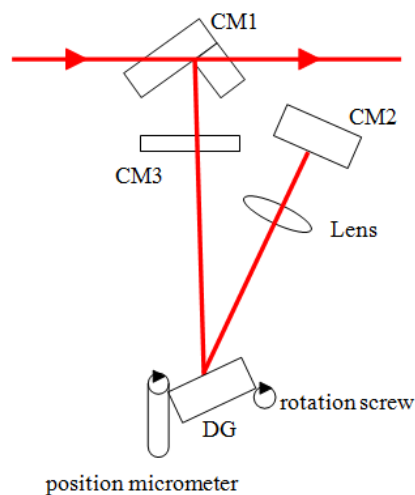


Fig. 2.4 Schematic setup of compressor in the "RegA 9000" laser system. CM1, CM2, CM3 are compressor optics. DG is the diffraction grating. The position micrometer allows adjustment of the grating along the mount's

Figure 2.5 a) and b) displays the autocorrelation curves of the 800-nm pulses measured with the pump-probe setup by adjusting the position micrometer and rotation screw, respectively. Figure 2.5 c) presents the pulse width compressed with 260 fs determined from a sech^2 fit.

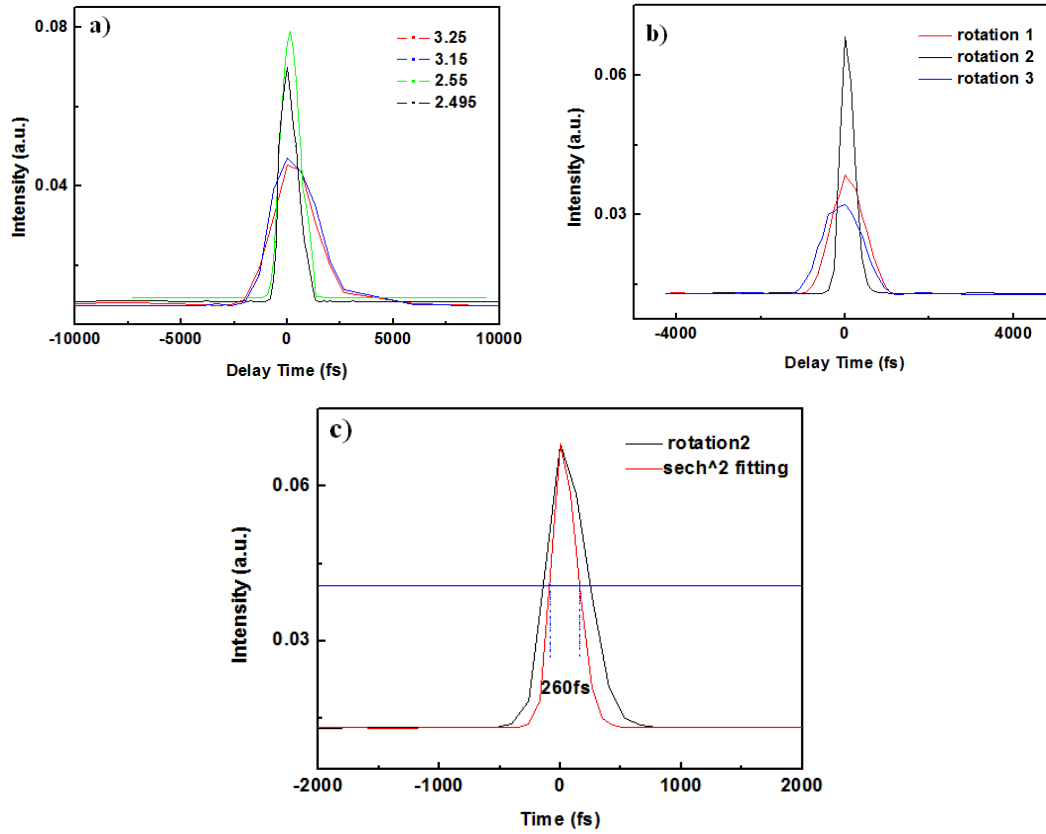


Fig. 2.5 Pulse duration adjusted by a) position micrometer (four different marked positions) and b) rotation screw (three rotations). Pulse duration is compressed and the pulse energy is increased with sharper peak. c) Pulse duration determined with sech^2 fitting for rotation 2.

2.3.2 MOKE and MSHG experimental setup

For MSHG experiment, the attenuated s-polarized beam (60 mW) selected by the polarizer is focused and incident on to the sample at an angle of 40 degree, as depicted in Fig. 2.6. The second-harmonic signal (400-nm wavelength) is generated along the direction of the reflected beam. The s-polarized component, in combination with a small p - component (around

6-degree rotation of the analyzer from *s*-polarization direction), is detected by the photo-multiplier tube (PMT). A high signal-to-noise ratio is obtained by using a lock-in amplifier and frequency-modulating the beam with the chopper. Filtering with prism is required to separate the MSHG light from the fundamental laser beam. Similar to MSHG experiment, MOKE signal is detected by the photodiode with *p*-in *s*-out combination.

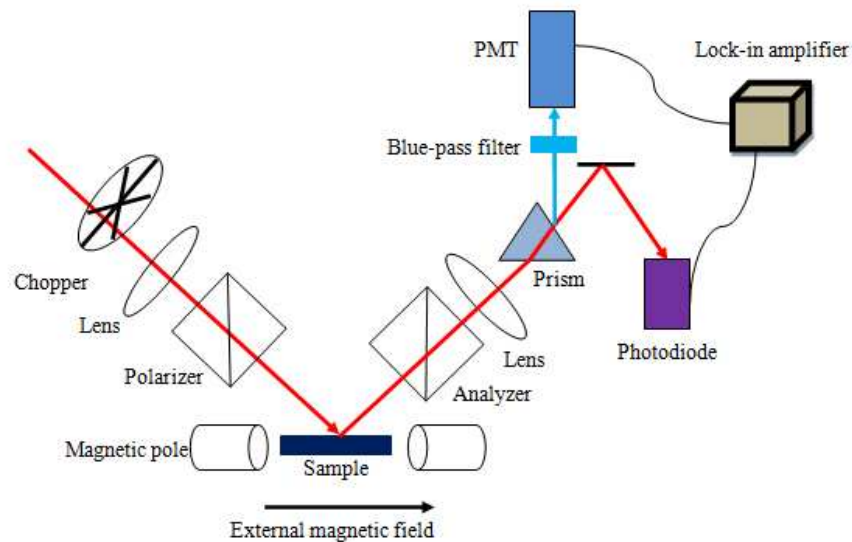


Fig. 2.6 Sketch of the MOKE & MSHG setup

Chapter 3

Magnetoelectric coupling in $\text{BaTiO}_3/\text{La}_{0.67}\text{Sr}_{0.33}\text{MnO}_3$ heterostructure

3.1 Introduction

Engineered thin-film heterostructures designed for electrical control of magnetic properties, the so-called magnetoelectric (ME) interfaces, present a novel route towards using the spin degree of freedom in electronic devices^{67,68}. Transition Metal Oxides (TMOs) are promising candidates for those multifunctional devices, due to their strong correlated electron system with coupled charge⁶⁹, spin⁷⁰ and orbital⁷¹ degrees of freedom. TMOs with the perovskite structure have a long history of research and have been known as materials with a variety of interesting properties, such as dielectric, magnetic, optical and transport properties^{40,72}. The interfaces of TMO heterostructures have the genuine property of breaking space inversion symmetry, and thus offer a unique and important test-bed to promote new phases and properties that can be controlled at atomic precision, such as conducting electron gases⁶⁹, superconductivity⁷³ or electric polarization dependent spin transfer^{49,74}. In recent years, there is enormous interest in the study of manganites, which are members of a broader set of compounds with strong correlated electrons. The $\text{R}_x\text{A}_{1-x}\text{MnO}_3$ series form a perovskite structure, where rare earth R^{3+} and alkaline earth A^{2+} cations occupy the corner of the cubic sites, while

manganese (Mn) cations occupy the center of the cubic sites, which is octahedrally coordinated with oxygen (Fig. 3.1). These compounds display large magneto-transport properties, the so called colossal magneto-resistance (CMR)^{75–81} and exhibit a variety of phases, with unusual, spin, charge, lattice and orbital order.

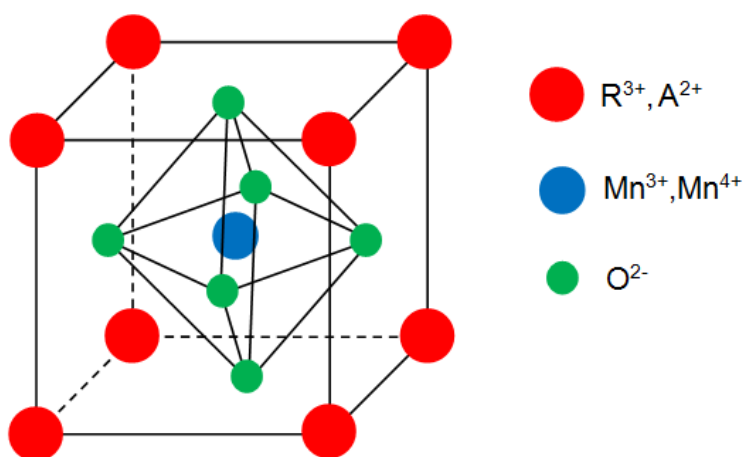


Fig. 3.1: Perovskite structure of compounds with chemical formula $R_xA_{1-x}MO_3$.

3.1.1 Motivation

The interfacial spin configuration of oxide heterostructures under electronic and structural reconstruction is key to emerging multiferroic (MF) and spintronic technologies with new functionality, and thus attracts research with different approaches^{38,82–85}. However, most experimental probes are indirect due to the lack of sufficient resolution to locate spin configuration at the

atomic scale. In this chapter, we use magnetization-induced second-harmonic generation (MSHG) to directly detect the interfacial magnetization controlled by the electric field with a series of BaTiO₃ (BTO)/La_{0.67}Sr_{0.33}MnO₃ (LSMO) samples.

3.1.2 Basic properties of La_{1-x}Sr_xMnO₃

The manganite La_{1-x}Sr_xMnO₃ has received much attention in the past decade. This material has a large Curie temperature, as high as 370 K at intermediate hole doping⁸⁶, and is widely considered as a representative of the "large-bandwidth"⁸⁷ family.

In La_{1-x}Sr_xMnO₃, the Mn ion is surrounded by the oxygen octahedron. The 3d orbitals on the Mn-site placed in such an octahedral coordination are subject to the partial lifting of the degeneracy by the crystal field. The lower-lying orbitals -- *t*_{2g} states are *d*_{xy}, *d*_{yz} and *d*_{zx}, while the higher-lying orbitals -- *e*_g states contain *d*_{x²-y²} and *d*_{3z²-r²} (Fig. 3.2)⁸⁸. The splitting energy is famously known as "10*Dq*"^{89,90}, and is between 1 and 2 eV usually. In the Mn³⁺ based compounds, all the 3d electrons are subject to electron repulsion interaction. Even the *e*_g state electrons, hybridized strongly with oxygen 2*p* states, are strongly affected by such a correlation effect, and tend to localize in the "carrier-undoped" compound, forming the so-called Mott insulator. However, the *e*_g electrons can be itinerant and play the role of conduction electrons, when electron vacancies or holes are created in the *e*_g

orbital states. This hole-doping procedure leads to the creation of Mn^{4+} ions. The transfer of electrons between two nearby Mn ions via the oxygen $2p$ orbital is known as double-exchange coupling in favor of ferromagnetic (FM) interaction⁹¹. The t_{2g} electrons, less hybridized with oxygen $2p$ states and stabilized by the crystal field splitting, are always localized by the strong correlation effect.

The important consequence of the apparent separation of the $3d$ orbital states is the effective strong coupling between the e_g conduction electron spins and t_{2g} localized electron spins. This on-site ferromagnetic coupling J_H is described as Hund's rule (Fig. 3.2)⁸⁸.

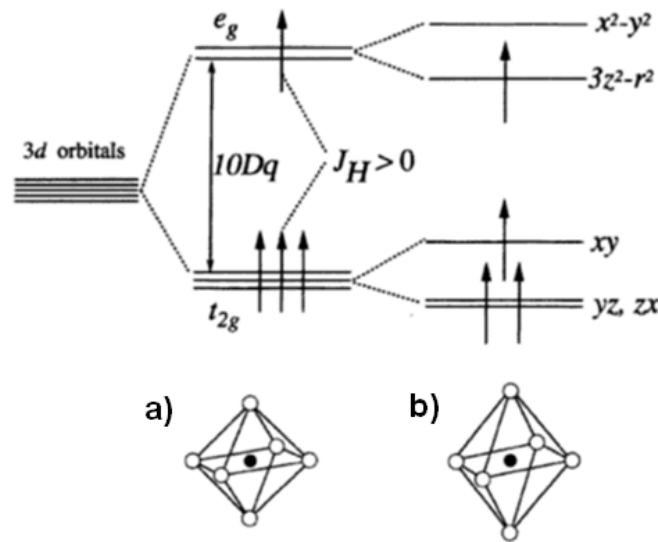


Fig. 3.2 Schematic representation of the crystal-field splitting of the $3d$ orbital of Mn ion. a) corresponds to the cubic, while b) corresponds to the tetragonal configuration with lattice spacing c (between the layers) larger than a and b (in plane of the layer).^[88]

The manganite LSMO exhibits a variety of phases (Fig. 3.3)^{86,92,93}. In the range from $x \sim 0.16$ to close to $x \sim 0.5$, the system at low temperature is in the FM state and exhibits metallic behavior mostly due to the double-exchange coupling. At large hole density, an antiferromagnetic (AFM) state is stabilized with A-type ordering. This state is actually FM-ordered within the x-y planes, and AFM-ordered only between planes. Within each plane, the orbital $d_{x^2-y^2}$ is lower in energy, producing a state with a uniform orbital order⁹⁴. The FM state of LSMO is intrinsically interesting due to the CMR phenomenon mentioned above and half-metallic property⁹⁵.

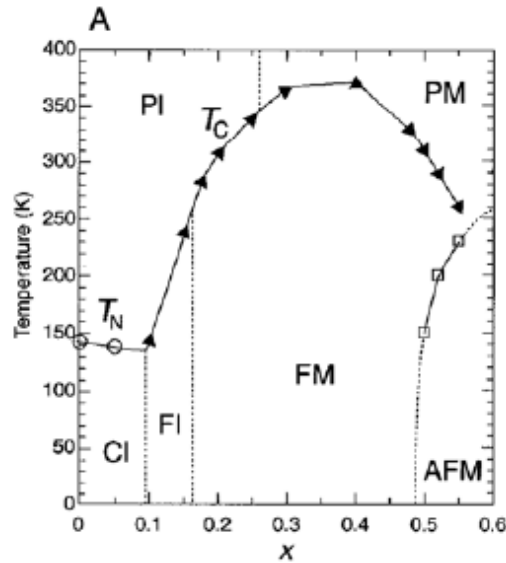


Fig. 3.3 Phase diagram of LSMO as concentration of Sr, courtesy of Y. Tokura and Y. Tomioka, prepared with data from reference 86 and 93. PM, PI, FM, FI and CI denote paramagnetic metal, paramagnetic insulator, FM metal, FM insulator, and spin-canted insulator states, respectively. T_C is the Curie temperature and T_N is the Néel temperature.^[92]

Half-metallic ferromagnets are systems where the spins of the electrons at the Fermi level have a particular direction: here, the spin-up electrons have a partially occupied band, while the electrons with opposite spin direction -- spin down, occupy filled bands separated from the unoccupied ones by a gap (Fig. 3.4)⁹⁴. Thus, half-metallic ferromagnets exhibit the coexistence of metallic behavior for spin-up electrons and insulating behavior for spin-down electrons. The electronic density of state (DOS) is completely spin-polarized at the Fermi level. It has 100% spin polarization for the conduction electrons theoretically^{96–98}, and thus offers potential technological applications such as single-spin electron source, and high-efficiency magnetic sensors.

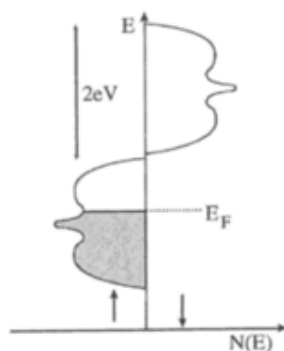


Fig. 3.4 Idealized density of states $N(E)$ for a half-metallic ferromagnetic. The Fermi energy is in the middle of a spin up band, but in between bands for the spin down band. ^[94]

3.1.3 Basic properties of BaTiO₃

Barium titanate, BaTiO₃ (BTO) is a perovskite-type ferroelectric with tetragonal symmetry, which possesses relatively large dielectric constant and electro-optic coefficient. BTO thin films have been proposed for applications in capacitors of dynamics random access memories and nonvolatile memories. BTO undergoes the structural phase transition from a high-temperature paraelectric phase into a low-temperature ferroelectric phase (Fig. 3.5)⁹⁹. The Curie temperature is about 120°C. BTO thin films that exhibit polarization-electric hysteresis loops have been successfully prepared by activated reactive evaporation¹⁰⁰, pulsed-laser deposition¹⁰¹ and sol-gel methods¹⁰². In addition to the polarization-electric hysteresis loop, the polarization switching by an electric field leads to a strain-electric field hysteresis loop, which resembles the shape of a butterfly¹⁰³, due to the piezoelectric effect of the lattice.

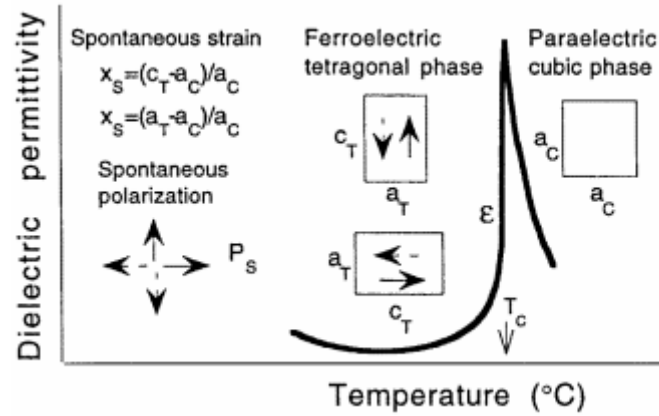


Fig. 3.5 Illustration of the changes of BTO transforms from a paraelectric cubic into ferroelectric tetragonal phase with temperature. The permittivity curve represents data measured on a BTO ceramic. The arrows show possible directions of the spontaneous polarization. The unit cell is represented by a square in the cubic phase and rectangle in the tetragonal phase. ^[99]

3.2 Samples and experiments

3.2.1 Sample preparation and characterization

The BTO (200 nm)/LSMO (50 nm) oxide heterostructures were grown on SrTiO₃ (001) substrates by using a multi-target pulsed-laser deposition system (KrF excimer laser 248 nm). The BTO (200 nm)/ LSMO (50 nm) epitaxial bilayer was deposited at a temperature of 750 °C in flowing oxygen of 300 mtorr pressure and cooled down in the same oxygen pressure (oxygen poor condition). The indium-tin-oxide (ITO) (50 nm) layer was deposited in situ at 50°C in 10 mtorr oxygen. In these cooling conditions, the saturation polarization of BTO is reduced from the full value due to oxygen vacancies¹⁰⁴.

Figure 3.6 shows the ferroelectric polarization of BTO with less saturation

value around $10 \mu\text{C}/\text{cm}^2$ as compared to the theoretical value $26 \mu\text{C}/\text{cm}^2$.^{105,106} A series of samples was fabricated, including inserting a 1-nm thick $\text{La}_{0.5}\text{Ca}_{0.5}\text{MnO}_3$ (LCMO) layer between BTO/LSMO and changing the oxygen vacancy concentration of BTO by in-situ annealing the sample in 600 mtorr O_2 at 450°C for 0.5 hour, making it O_2 richer than previous ones. The interfaces of the perovskite layers of a similar sample were characterized by scanning transmission electron microscopy (STEM) with aberration correction and low-loss electron energy loss (EELS) spectroscopy (Fig. 3.7)⁴⁹. STEM imaging of the interface region of an as-grown multilayer reveals a continuous barrier layer.

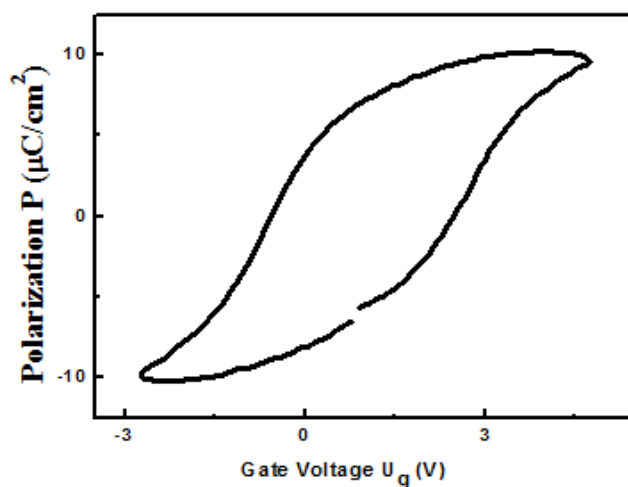


Fig. 3.6 Ferroelectric polarization hysteresis loop of BTO from oxygen poor BTO/LSMO sample.

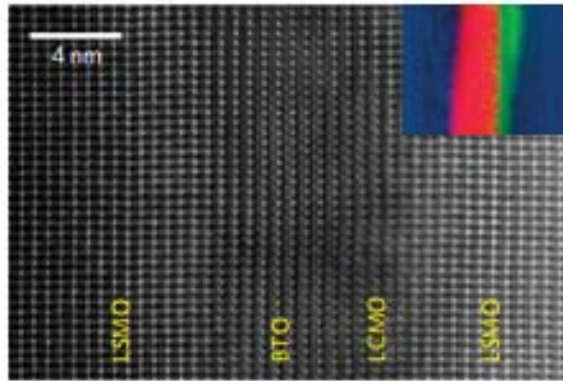


Fig. 3.7 Cross-sectional annular dark-field STEM image at the interface region of LSMO/BTO/LCMO/LSMO tunnel junction. The inset is the low-loss (EELS) map representing spectroscopic signatures of LSMO (blue), BTO (red) and LCMO (green).^[49]

3.2.2 MSHG and MOKE experiments

All optical experiments are performed at 80 K below the Curie temperature by placing the samples in a cryostat cooled by liquid nitrogen. MSHG is used to characterize the interfacial magnetic property and Magneto-Optical Kerr effect (MOKE) is carried out to characterize the bulk magnetic property. To study the interfacial ME coupling effect, an external magnetic field is applied in plane, and an external electric field is applied out of the plane using a "Keithley 2400 Sourcemeter" (Fig. 3.8).

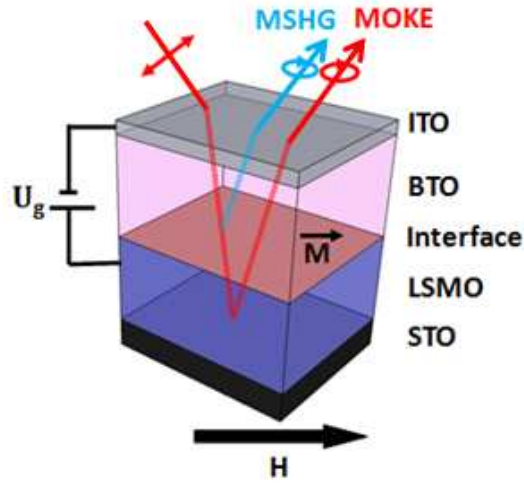


Fig. 3.8 Schematic of the optical measurements. MOKE measures the bulk magnetization of the LSMO film, while MSHG selectively probes the interface magnetization only. LSMO and ITO are two electrodes where a voltage is applied.

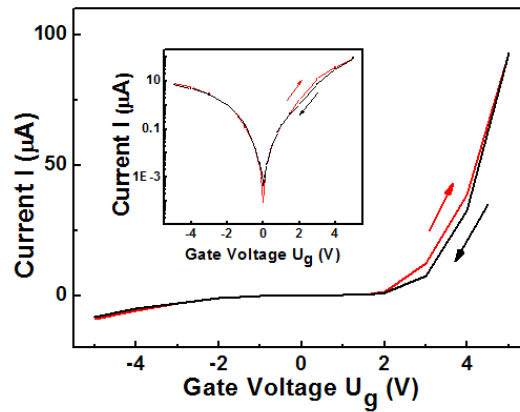


Fig. 3.9 I-V curve of oxygen poor BTO/LSMO sample at 80 K. Inset is the semi-log current curve.

Figure 3.9 exhibits the Current-Voltage (I-V) curve measured from the oxygen-poor BTO/LSMO sample at 80 K. A typical diode effect is revealed,

indicating that a Schottky contact is formed at the BTO/LSMO interface (Fig. 3.10). The oxygen vacancies introduced by the oxygen-poor growth process make the BTO n-type. The electron depletion (or accumulation) with the applied field will play an important role in the interfacial ME effect.

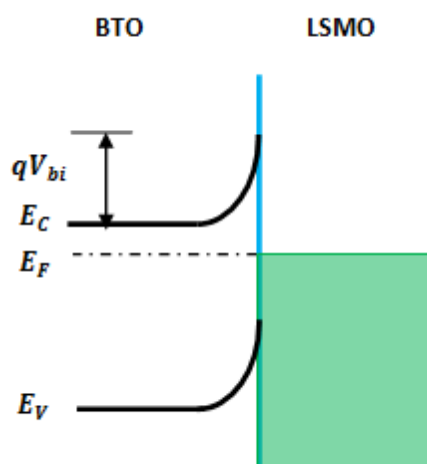


Fig. 3.10 Schematic band diagram of the n-type Schottky contact. E_C , E_V , E_F and V_{bi} denote conduction band, valence band, Fermi level and build-in potential, respectively.

3.3 Results

3.3.1 Interfacial magnetic transition induced by magnetoelectric effect

MSHG is used to selectively probe the interface of oxygen-poor BTO (200 nm)/LSMO (50 nm) sample. Figure 3.11 shows the voltage dependent MSHG hysteresis loops varying from -4V to +4V. When the gate voltage U_g is below a critical voltage $U_c = +1V$, MSHG hysteresis loops are observed. However, they vanish at higher positive voltage. To illustrate the phenomenon

in detail, the MSHG contrast A is calculated for each loop and the voltage-dependent contrast curve is displayed in Fig. 3.12 (red curve). For $U_g < U_c$ (+1 V), the interfacial LSMO is in the FM state since the magnetic contrast is obvious. Above U_c the magnetic contrast A suddenly vanishes. A reversible transition is observed by varying the gate voltage from +4V back to initial value of -4V (Fig. 3.12 black curve). We attribute this sudden, reversible FM-to-AFM phase transition to an interface ME effect.

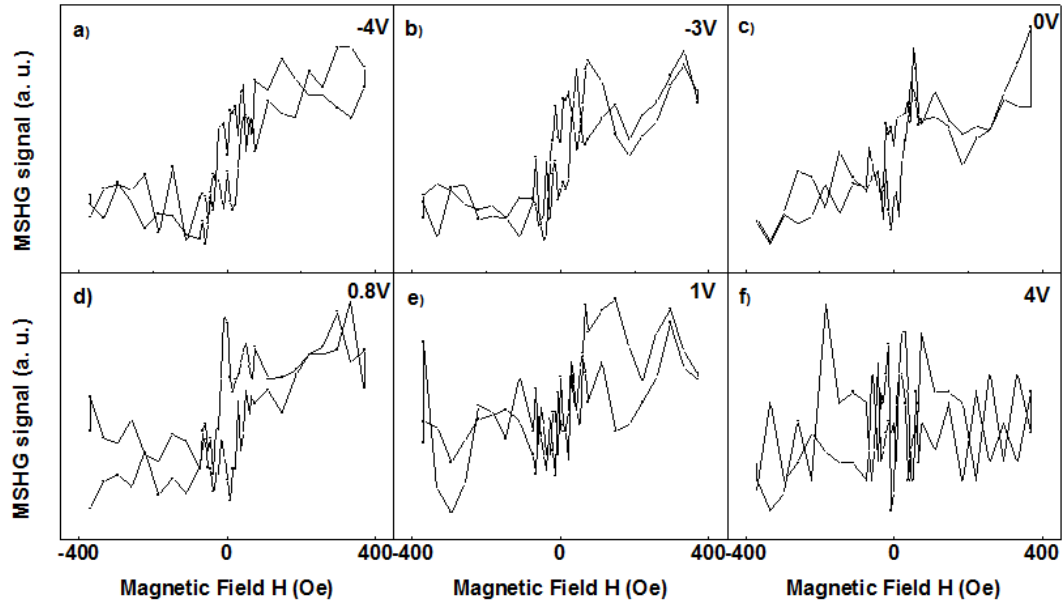


Fig. 3.11 MSHG hysteresis loops at different voltage.

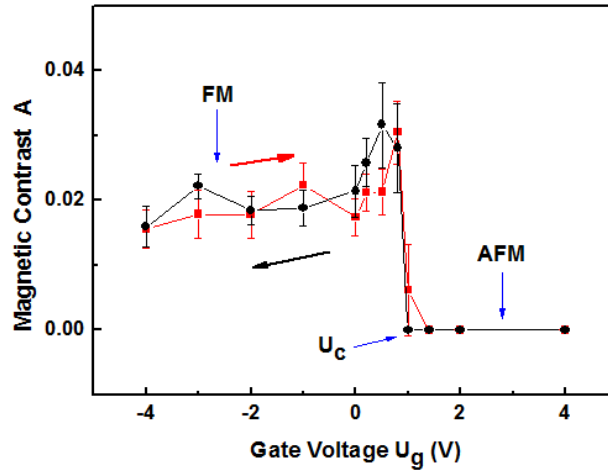


Fig. 3.12 Magnetic contrast A determined from MSHG measurements as a function of gate voltage U_g .

MOKE experiments are also performed to detect the bulk property of LSMO. Figure 3.13 displays the MOKE hysteresis loops at different voltage. MOKE contrast A as a function of gate voltage U_g is shown in Fig. 3.14. The MOKE loops remain constant over the whole voltage range. Also, the contrast A does not show much change. This demonstrates that the ME coupling has no effect on the bulk magnetic property, and that it constitutes an interfacial effect.

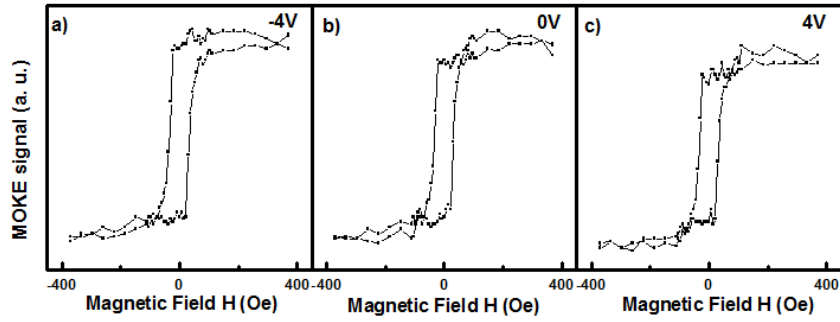


Fig. 3.13 MOKE hysteresis loops at different voltage

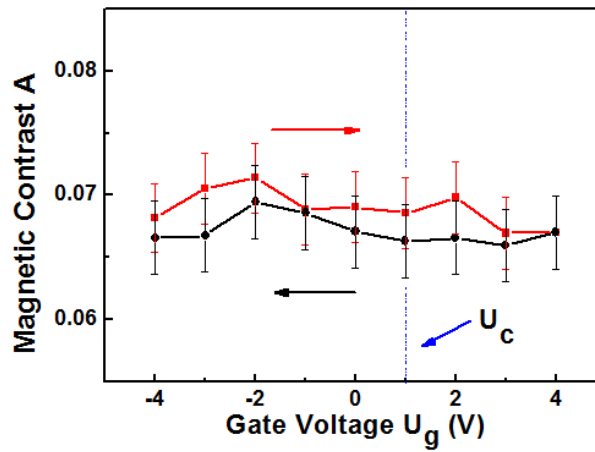


Fig. 3.14 Magnetic contrast A determined from MOKE measurements as a function of gate voltage U_g .

3.3.2 Voltage-dependent second-harmonic generation

Furthermore, SHG as a function of gate voltage is measured. Figure 3.15a exhibits the $P_{in}P_{out}$ SHG intensity. P_{in} refers to P-polarized fundamental electric

field, while P_{out} denotes P-polarized SHG field. To illustrate the data more clearly, we square-root and normalize the $P_{in}P_{out}$ SHG data, and compare it to the P-V loop, as shown in the inset of Fig. 3.15a. The $P_{in}P_{out}$ SHG data has similar trend as the ferroelectric polarization but with much smaller coercivity. We conclude that the $P_{in}P_{out}$ SHG signal mainly arises from BTO and the voltage-dependent signal is manipulated by the polarization of BTO. The much smaller coercivity of the $P_{in}P_{out}$ loop indicates the weakness of ferroelectricity. One possible explanation is that the ferroelectricity is weakened exponentially with size. At 80 K, the bulk BTO is tetragonal and the surface tends toward the cubic phase, and the disordered nonpolar layers would become paraelectric¹⁰⁷. If the $P_{in}P_{out}$ SHG signal is generated in a few monolayers near the BTO/LSMO interface, it would exhibit, at best, very weak ferroelectric-like hysteresis. The training effect (no overlap at negative voltage of $P_{in}P_{out}$ SHG curves with increasing and decreasing voltage) can be attributed to electrical-insulation degradation of the $BaTiO_3$ layer due to electrotransport of oxygen vacancies¹⁰⁸, which would further weaken the ferroelectricity at the interface. Figure 3.15b shows the $S_{in}S'_{out}$ SHG signal. S' refers to S-polarization component mixed with small P-polarization component. Different from $P_{in}P_{out}$ signal, it almost vanishes rather than increases for $U_g > U_c$. Therefore, the $S_{in}S'_{out}$ signal does not arise from the BTO layer, and is instead generated by the LSMO interfacial layer. The zero point represents the flatband voltage $U_f = +1.4$ V, indicating that the FM-to-AFM phase transition occurs in a bias regime of electron injection

and hole accumulation at the BTO/LSMO interface.

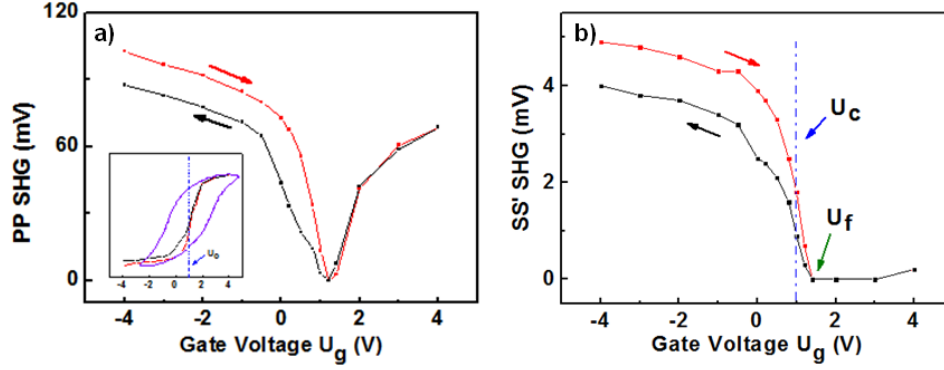


Fig. 3.15 a) $P_{in}P_{out}$ SHG signal measured at 80 K and the inset shows a comparison between the square-rooted $P_{in}P_{out}$ SHG curve (labeled in black and red) and the P-V loop (labeled in violet). b) $S_{in}S'_{out}$ SHG signal measured at 80 K.

3.3.3 Effect of $\text{La}_{0.5}\text{Ca}_{0.5}\text{MnO}_3$ interlayer

A giant tunnel electroresistance ratio by inserting a thin (nanometer) $\text{La}_{0.5}\text{Ca}_{0.5}\text{MnO}_3$ layer has been observed recently¹⁰⁹. Here, BTO(200 nm)/LCMO(1 nm)/LSMO(50 nm) is studied with MSHG and MOKE characterization. The I-V curve shows good diode effect (Fig. 3.16). Figure 3.17 displays the MSHG signal at different applied voltages. Similar interface magnetization transition is observed and the magnetic contrast is calculated and represented in Fig. 3.18. The magnetic contrast is enhanced as compared to the sample without LCMO interlayer.

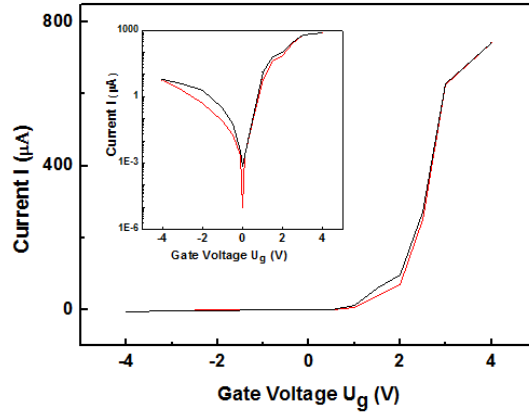


Fig. 3.16 I-V curve of oxygen-poor BTO/LCMO/LSMO sample. Inset represents I-V curve on log scale.

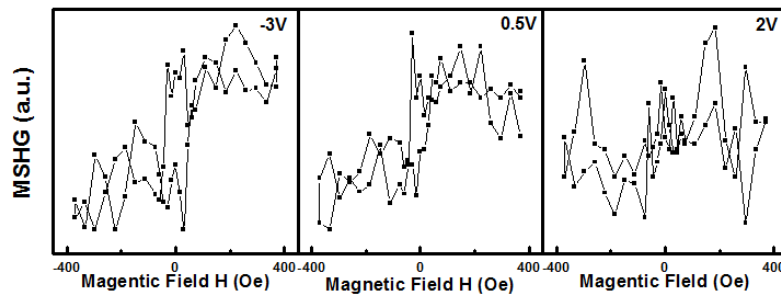


Fig. 3.17 Hysteresis loops with different voltage applied.

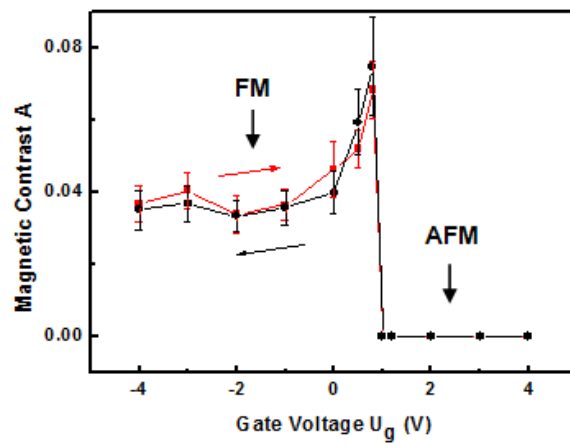


Fig. 3.18 Magnetic contrast as a function of gate voltage U_g .

SHG as a function of voltage are also measured (Fig. 3.19). $P_{in}P_{out}$ SHG signal shows similar trend as the BTO/LSMO sample (Fig. 3.19a). However, the signal rises above the critical positive voltage for $S_{in}S'_{out}$ signal (Fig. 3.19b). We attribute this to the LCMO interlayer which enhances the voltage-dependent SHG response. Thus we need to confirm from which part the MSHG signal originates. We use a BTO/LCMO bilayer without LSMO as a reference sample. The hysteresis loop of BTO/LCMO measured with MOKE shows larger coercivity field $H_c=350$ Oe (Fig. 3.20a) as compared to LSMO coercivity field $H_c=35$ Oe (Fig. 3.20b). The coercivity of BTO/LCMO/LSMO sample measured with MSHG is almost equal to that of bulk LSMO (Fig. 3.20b). Thus we exclude the magnetic contribution of LCMO to MSHG signal and conclude that the interfacial magnetic transition occurs in the LSMO layer at positive gate voltage.

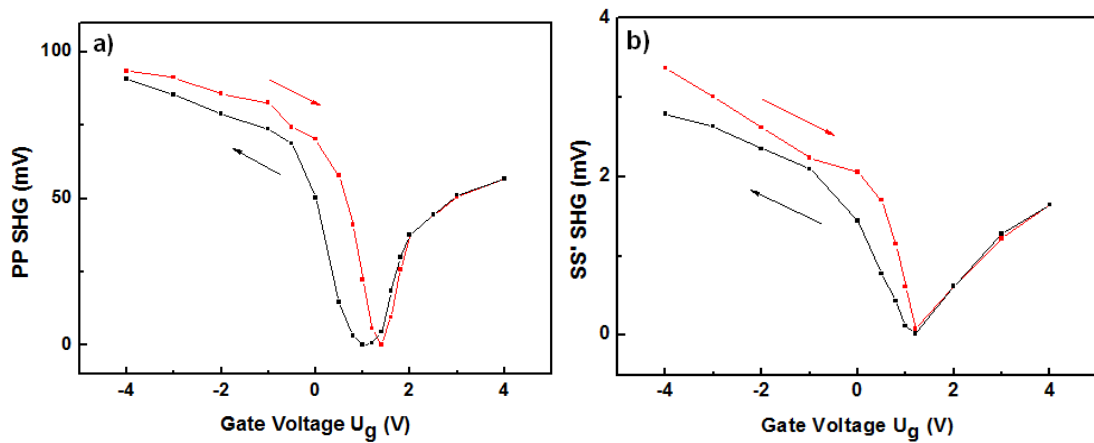


Fig. 3.19 a) $P_{in}P_{out}$ SHG signal and b) $S_{in}S'_{out}$ signal as a function of gate voltage U_g .

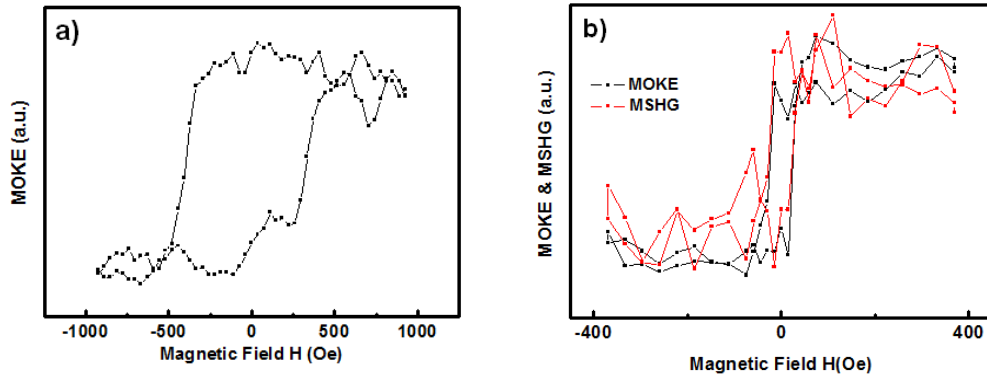


Fig. 3.20 a) MOKE hysteresis loop of BTO/LCMO at 80K and b) Comparison of coercivities between MOKE and MSHG of BTO/LCMO/LSMO at 80 K.

A thinner BTO (100nm)/LCMO/LSMO multilayer sample is also investigated. MSHG and MOKE hysteresis loops are displayed in Fig. 3.21a) and b) respectively for different voltages. The MSHG contrast is calculated and is displayed in Fig. 3.22. The transition voltage $\sim 1V$ is almost the same as for the thicker sample which further indicates that there is almost no modulation induced by the ferroelectric property of BTO.

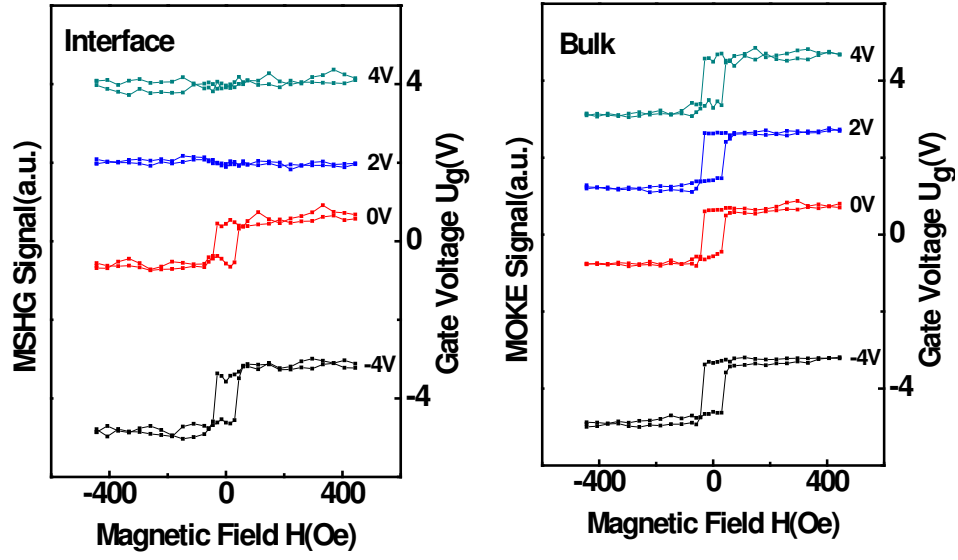


Fig. 3.21 a) MSHG and b) MOKE hysteresis loops with different voltage applied

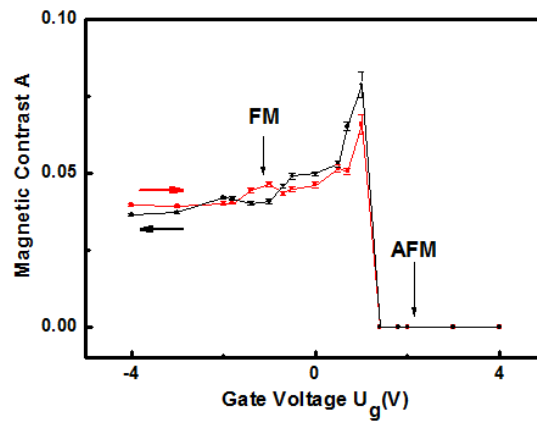


Fig. 3.22 Magnetic contrast as a function of gate voltage U_g .

3.3.4 Effect of dopants in BaTiO₃ layer

Further evidence for the ME coupling mechanism is provided from dopant dependent studies of the BTO layer. BTO (200nm)/LSMO (50nm) under oxygen rich condition is prepared. C-V measurements (Fig. 3.24a) reveal that the oxygen rich sample has a lower electron concentration of $8 \times 10^{17} \text{ cm}^{-3}$ (Fig. 3.24b) as compared to that of oxygen poor sample (Fig. 3.). MSHG measurements at a variety of gate voltages are performed (Fig. 3.25) and the interface magnetic transition of the oxygen-rich sample is shifted to a much higher gate voltage $U_g = +6 \text{ V}$, as shown in Fig. 3.26. We note that the P-V curve of oxygen-rich sample (Fig. 3.23b) is comparable to the oxygen-poor sample, indicating further that the magnetic transition is not driven by the FE polarization. In contrast, the I-V characteristic of the oxygen-rich sample exhibits a much higher threshold voltage for the onset of current flow across the heterojunction, as shown in Fig. 3.23a. The $S_{\text{in}}S'_{\text{out}}$ SHG illustrates that there is much smaller electric field at the interface and a higher voltage is needed to cause the interfacial magnetic transition (Fig. 3.27). We attribute this to the lower electron (oxygen vacancy) concentration of the oxygen rich sample. This demonstrates that the electric field at the heterojunction is crucial for the observed interface ME coupling effect.

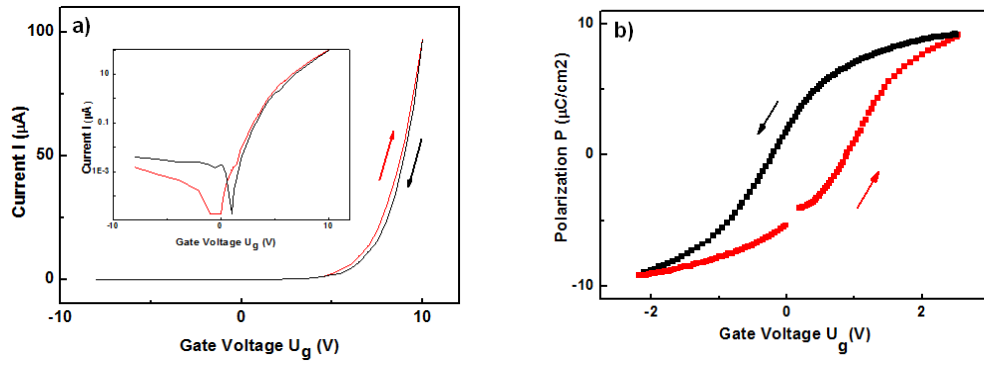


Fig. 3.23 a) I-V curve, inset is semi-log curve. b) P-V curve.

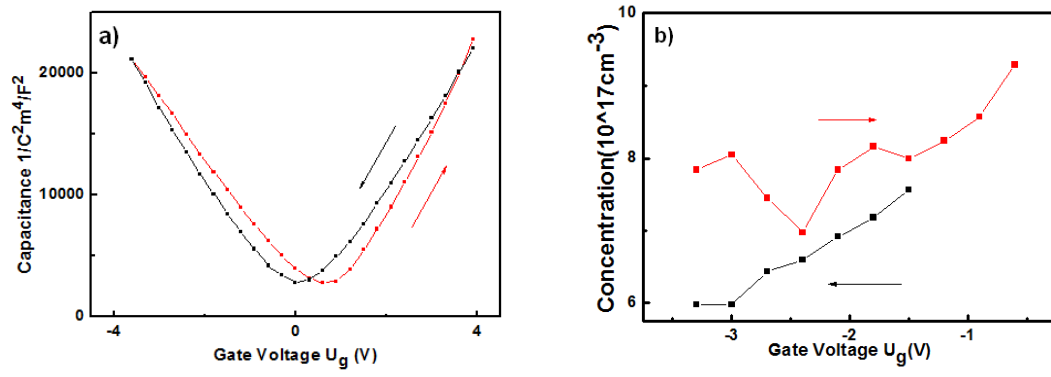


Fig. 3.24 a) C-V curve; b) Carrier concentration calculated from C-V measurement.

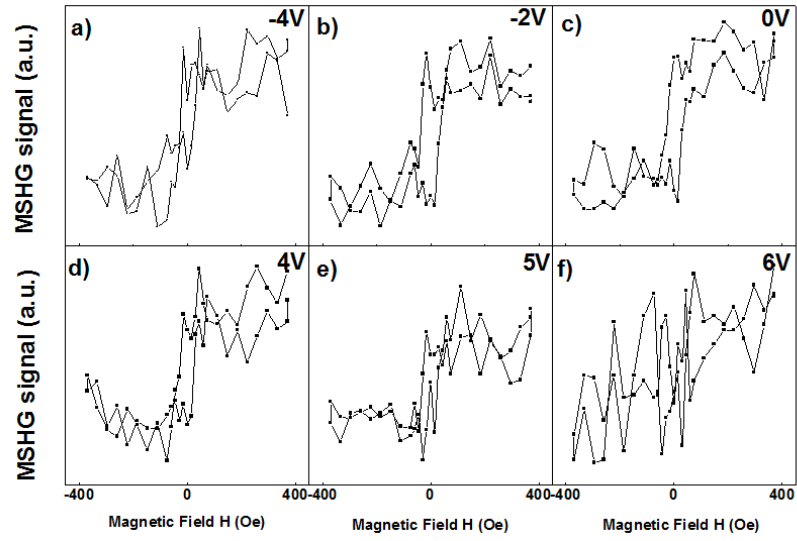


Fig. 3.25 MSHG hysteresis loops at a series of voltage.

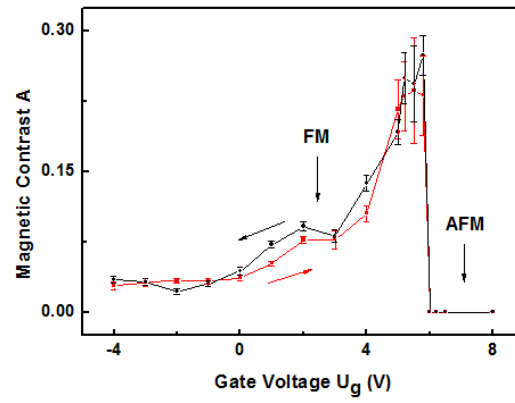


Fig. 3.26 MSHG magnetic contrast as a function of gate voltage U_g .

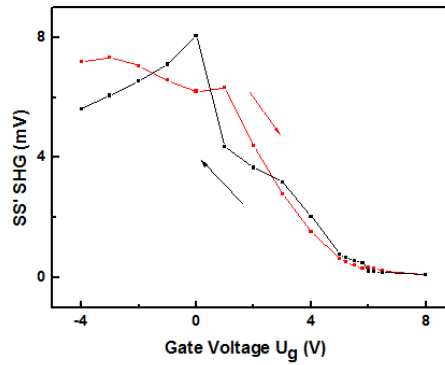


Fig. 3.27 $S_{in}S'_{out}$ SHG as a function of gate voltage U_g .

3.4 Discussion

Several mechanisms have been explored to achieve interfacial magnetoelectric coupling in artificial multiferroic heterostructures and composites: strain, spin-exchange, and charge coupling^{110–113}. In the following sections, these mechanisms will be discussed with respect to BTO/LSMO heterostructure.

3.4.1 Possible mechanisms for interfacial magnetoelectric effect

The lattice constant of BTO can be modulated by the external electric field due to its piezoelectricity. It is the ability of the single crystal to develop an electric charge proportional to a mechanical stress or to produce a deformation proportional to an electric field. The in-plane and out-of-plane lattice distortions are defined as:

$$\frac{(a-a_0)}{a_0} = d_{31}E , \quad (3.1)$$

$$\frac{(c-c_0)}{c_0} = d_{33}E , \quad (3.2)$$

where a_0 and c_0 are lattice constant at zero field, E is the electric field. Here, we assume that the piezoelectric-modulated strain in BTO is transferred onto the LSMO lattice at the interface. This assumption might lead to a larger estimation of the LSMO lattice distortion, but is still similar with realistic case. The average distortion of BTO $d_{31}=-82$ pm/V is used¹¹⁴ and the calculated strain in LSMO at +4V is about 1.64%. From the work of reference 102, the butterfly shaped strain hysteresis loops are observed¹⁰³ with the application of

an electric field, which is not consistent with the voltage dependence of the interface magnetization transition. Thus the strain would not play an important role for this effect.

Modulation in the charge carrier density can lead to profound modifications in the magnetic interactions by directly perturbing the relative weight of the kinetic and Coulomb energy terms of the system⁶⁸. The ferroelectric property of BTO can modulate the charge density at the interface. The charge-mediated mechanism is depicted by a model of screening charge accumulation at the BTO/LSMO interface. When the electric displacement is pointing away from the interface, the electron depletion (hole accumulation) occurs. Otherwise, the electron accumulation (hole depletion) would occur at the interface. Considering the boundary condition at the interface, the charge distribution is expressed as $D\delta(z)$, where D is the electric displacement at the interface and z is the distance away from the interface. The density of charge at the LSMO side exponentially decays with increasing distance away from the interface. Thus the charge distribution can be expressed as $D\delta(z) - \frac{D}{\lambda}e^{-\frac{z}{\lambda}}$, where $\lambda = 4.14\text{\AA}$ is the Thomas-Fermi screening length of LSMO¹¹⁵. The modulation of hole doping level per Mn ion in the first unit cell at the interface is approximately calculated by integration of the charge distribution over a distance from the interface to one lattice constant in LSMO. The saturation polarization of BTO is about $10\text{ }\mu\text{C}/\text{cm}^2$ from Fig. 3.6. Thus, the ferroelectric polarization would contribute to the hole injection with the

maximum value $H_{FE} = 0.044 e/u.c.^2$. The magnetization transition from FM to AFM occurs around 0.5 doping level in LSMO, which means a hole doping level of $0.167 e/u.c.^2$ per Mn ion is required to achieve the magnetization transition. The ferroelectric effect of modulated hole doping is far too small, indicating that it would not dominate the hole injection in our case. The P-V curve (Fig. 3.6) suggests that the observed interface magnetic transition is not caused by polarization switching of the BTO layer. There is no sudden jump in the P-V curve, nor does the magnetic contrast A exhibit a hysteresis loop (Fig. 3.12). The observed interface ME effect is therefore not related to the polarization-induced interface magnetic transition of LSMO, as observed for PZT/LSMO interface^{38,116}.

The diode effect (Fig. 3.9) is shown on this sample. Thus the electric displacement at the interface is not only caused by the ferroelectric polarization effect, but also originates from the band bending. The characteristic quantities of the Schottky contact can be deduced by solving Poisson's equation^{117,118}. The maximum electric field at the interface E_m is given by^{119,120}:

$$E_m = \sqrt{\frac{2qN_{eff}|V-V_{bi}|}{\epsilon_0\epsilon_{st}}} \pm \frac{P}{\epsilon_0\epsilon_{st}}, \quad (3.3)$$

where V_{bi} is the build-in potential, N_{eff} is the effective charge density in the depletion region. P , q , ϵ_0 and ϵ_{st} denote ferroelectric polarization, electron charge, permittivity of the free space and low frequency (static) dielectric constant of the ferroelectric layer, respectively. Then the electric displacement

is given by:

$$D = \varepsilon_0 \varepsilon_{st} E_m = \sqrt{2q\varepsilon_0 \varepsilon_{st} N_{eff} |V - V_{bi}|} \pm P . \quad (3.4)$$

Capacitance measurements are done to estimate the charge density of the sample (Fig. 3.28). For a Schottky contact, the capacitance is related to the voltage by^{119,120}:

$$\frac{1}{C^2} = \frac{2}{q\varepsilon_0 \varepsilon_{st} N_{eff}} |V'_{bi} - V| . \quad (3.5)$$

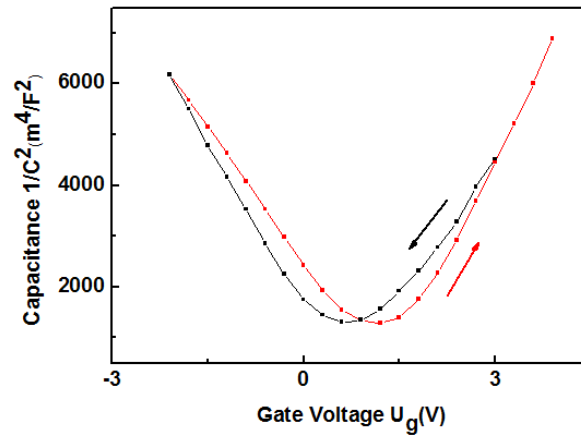


Fig. 3.28 Capacitance as a function of gate Voltage U_g

From the C-V measurement, the doping density can be evaluated, according to^{119,120}:

$$N_{dop} = \frac{2}{q\varepsilon_0 \varepsilon_{st} [d(1/C^2)/dV]} . \quad (3.6)$$

It is important to point out that N_{dop} is the density of free carriers to follow the small ac probing voltage used to measure capacitance. The effective charge density used in the theoretical equation of the capacitance includes not only

the free carriers but also the fixed charges in the space charge region. Therefore, we should expect the $N_{eff} > N_{dop}$. Figure 3.29 displays the doping concentration calculated from C-V curve.

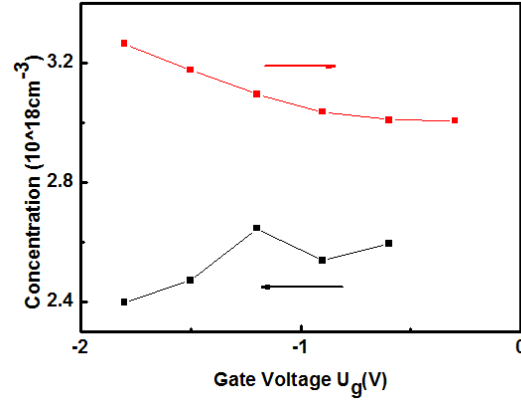


Fig. 3.29 Concentration of oxygen poor sample

In general, the build-in potential can also be evaluated from the slope and intercept values based on the C-V characteristics. In our case, the ferroelectric effect also contributes to the build-in potential. The large range of reversal of ferroelectric polarization makes it not proper to determine the build-in potential directly from the C-V curve. Here, we determine the build-in potential V_{bi} from the I-V characteristics, according to^{119,120}:

$$I = AA^*T^2 \exp\left(-\frac{q}{kT}\left(\Phi_B - \sqrt{\frac{qE_m}{4\pi\epsilon_0\epsilon_{op}}}\right)\right). \quad (3.7)$$

For large applied voltages, the expression becomes $\ln(I) \sim (V - V_{bi})^{1/4}$. The build-in potential is chosen to obtain the best linear fit (Fig. 3.30).

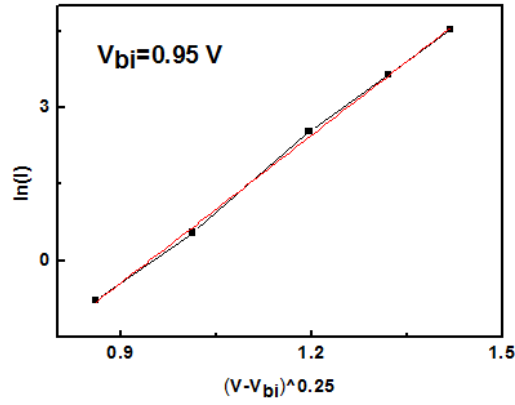


Fig. 3.30 Linear fitting to determine the build-in potential.

Here, another mechanism is possible to modulate the interface magnetization with the injection of the minority spins. As shown schematically in Fig. 3.31a, at the reverse gate voltage U_g , no spin injection current occurs at the n-type BTO/LSMO interface. The nearby majority spins of Mn^{3+} and Mn^{4+} ions are double-exchange coupled, leading to a ferromagnetic state. When a forward-bias voltage is applied, electron depletion at the interface reduces the number of e_g electrons per Mn ion, weakening the FM configuration due to less spin hopping. In this case, the most important process is the minority spin injection from BTO to LSMO layer near the interface, as depicted in Fig. 3.31b. The majority spins flow across the LSMO layer by spin-hopping process t . In contrast, the minority spin-down electrons will accumulate at the interface, since the spin-hopping process t is blocked by the strong interaction with the local spins due to the large Hund's rule coupling J_H . Hence, the minority spins accumulate at the first layer near the interface rather than flowing across the

LSMO layer as the majority spins. Thus, the super-exchange interaction of t_{2g} electrons between neighboring Mn ions favor the AFM configuration near the interface. At a critical gate voltage U_c , a FM-to-AFM phase transition occurs at the BTO/LSMO interface. In contrast, the LSMO bulk maintains the FM configuration due to the double-exchange interaction as the minority spins are confined to the interface.

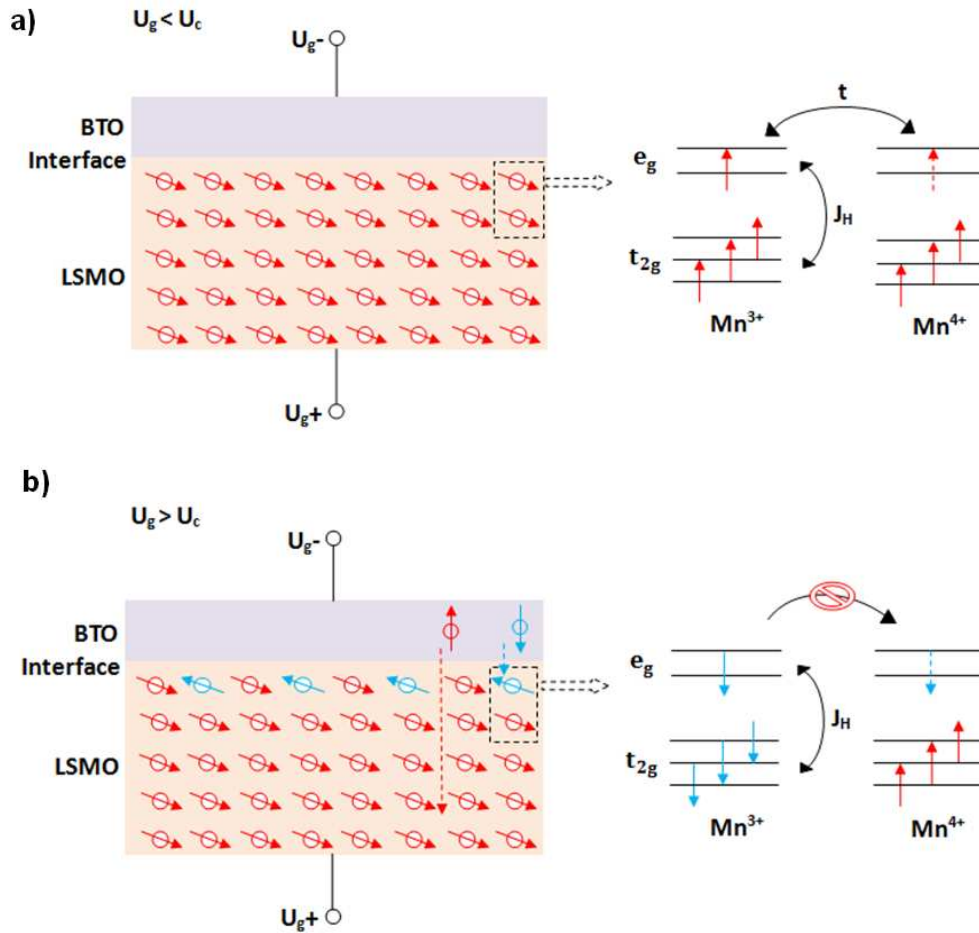


Fig. 3.31 Schematic model of spin alignment at BTO/LSMO interface. a) Below critical gate voltage U_c , majority spins (red arrows) of Mn^{3+} and Mn^{4+} ions are double-exchange coupled (right panel), leading to a ferromagnetic state of LSMO. b) Above U_c , The AFM super-exchange interaction of t_{2g} electrons between neighboring Mn ions dominates, and the interfacial LSMO layer undergoes a FM-to-AFM phase transition.

3.4.2 Microscopic mechanism for interfacial magnetoelectric effect

Next, we will discuss the microscopic mechanism of this novel interface ME effect. Figure 3.32 shows a schematic of the proposed magnetic structure and band alignment at the n-type BTO/LSMO Schottky junction with positive gate voltage. For FE polarization (P) pointing away from the LSMO layer, the hole accumulation biases the interfacial LSMO layer towards the AFM insulating phase. The $\text{La}_{0.7}\text{Sr}_{0.3}\text{MnO}_3$, however, has stoichiometry that is far enough from the phase boundary and a change in magnetic order is not expected owing solely to a build-up of screening charge¹⁰⁹. On the other hand, for a positive gate voltage applied to the LSMO layer, an electron current (J) begins to flow across the BTO/LSMO heterojunction. Both, spin-up and spin-down electrons will be injected from the conduction band of BTO into the interfacial LSMO layer, since the spin polarization of LSMO surfaces extracted from transport measurements usually yield less than 95%¹²¹. The majority spin-up electrons will quickly relax to the Fermi level and conduct through the LSMO layer. In contrast, the minority spin-down electrons will accumulate at the interface, since the spin-hopping process t is blocked by the strong interaction with the local spins due to the large Hund's rule coupling J_H . This will weaken the double-exchange mechanism and hence reduce the ferromagnetic coupling between Mn ions at the LSMO interface. At a critical gate voltage U_c , the injected minority spin-down electrons will reduce the double-exchange mechanism such that the AFM super-exchange interaction

will dominate, and the interfacial LSMO layer will undergo a FM-to-AFM phase transition. This magnetic reconstruction will occur in the few Mn layers at the interface, since the minority spin-down electrons will strongly scatter with electrons, phonons and magnons, resulting in fast spin-flip processes¹²². The magnetic reconstruction at the interface also leads to spin frustration, with the competition between AFM coupling at the interface and FM ground state of bulk LSMO. To achieve a more energetically favorable state, the spins in the interfacial layer will cant along the spin direction of the bulk LSMO.

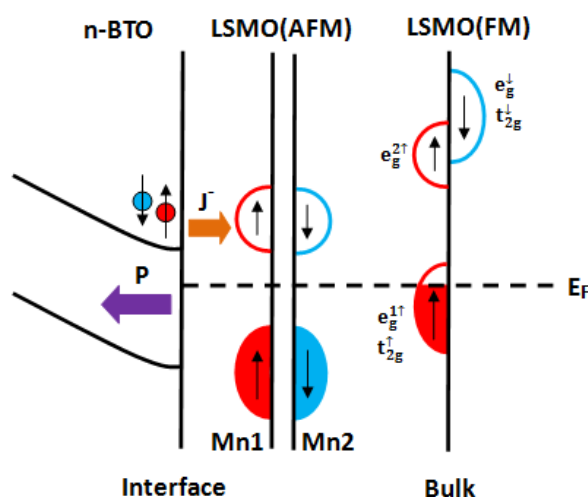


Fig. 3.32 Schematic band diagram of the n-type BTO/LSMO Schottky junction for $U_g > U_c$, depicting the electron current J^- , ferroelectric polarization P , and considering an AFM-ordered LSMO interface layer and a half-metallic LSMO electrode with only spin-up states at the Fermi level E_F .

Chapter 4

Magnetoelectric coupling in $\text{SrTiO}_3/\text{La}_{0.5}\text{Ca}_{0.5}\text{MnO}_3/\text{La}_{0.67}\text{Sr}_{0.33}\text{MnO}_3$ heterostructure

4.1 Introduction

To elucidate further the observed magnetoelectric (ME) effect, a non-ferroelectric system - $\text{SrTiO}_3/\text{La}_{0.5}\text{Ca}_{0.5}\text{MnO}_3/\text{La}_{0.67}\text{Sr}_{0.33}\text{MnO}_3$ - is studied in this section.

4.1.1 Basic properties of SrTiO_3

Strontium titanate SrTiO_3 (STO) is a good candidate. It is paraelectric with a relative dielectric constant as high as 300 at room temperature^{123,124} and has been widely studied due to its variety of applications¹²⁵. Stoichiometric STO with a simple-cubic perovskite structure is an insulator at room temperature with a band gap of 3.2 eV. The Ti^{4+} ion at the cubic body center is surrounded by O^{2-} ions at the face center sites and Sr^{2+} ions at the cubic corners. As the temperature is reduced the crystal structure becomes tetragonal at 110 K, and at 65 K the structure becomes orthorhombic¹²⁶. However, the electrical property in the bulk STO can be changed with oxygen vacancy^{127,128} or impurity doping, such as Nb or La^{129,130}. From the viewpoint of conductivity, STO can be changed from an insulator to a n-type semiconductor and finally to a metallic conductor. In

the region of thin-film growth, STO is very often used as the substrate for depositing other perovskite oxides owing to the small in-plane lattice mismatch¹³¹. Because of its notable dielectric and doped semiconducting properties, STO can be utilized to develop field-effect devices¹³² besides the application in dynamic random-access memories, and high-density capacitors.¹³³

4.1.2 Basic properties of $\text{La}_{1-x}\text{Ca}_x\text{MnO}_3$

$\text{La}_{1-x}\text{Ca}_x\text{MnO}_3$ (LCMO) is among the most-studied compounds of the manganite family due to its robust magnetoresistance effect¹³⁴, larger than in other much-studied materials such as $\text{La}_{1-x}\text{Sr}_x\text{MnO}_3$ (LSMO). The Ca ionic size is almost identical to the La ionic size, and thus a true solid solution forms in the entire range of Ca concentrations. Antiferromagnetic (AFM) superexchange coupling exists between Mn^{4+} ions via an intervening oxygen, while the superexchange interaction with a Mn^{3+} ion can be AFM or ferromagnetic (FM) depending on the relative orbital orientation. The real hopping between Mn^{3+} and Mn^{4+} through an oxygen produces a FM coupling via the double exchange mechanism⁹¹. Therefore, it is expected that there exists close interplay among charge carriers, magnetic couplings, and structural distortions in LCMO. The phase diagram is depicted in Fig. 4.1⁸⁸. Both perovskites LaMnO_3 and CaMnO_3 are AFM insulators. The prominent phase is the FM low-temperature metallic state for Ca concentration of 0.2 ~

0.5 caused by the double exchange coupling. CMR behavior is displayed in this region¹³⁵. The ferromagnetism, optimized at $x = 3/8$, persists up to $x \approx 0.5$, charge ordering becomes stable for $x > 1/2$, and there exists a remarkable competition between ferromagnetism and charge ordering at Ca concentration of 1/2. The compound $\text{La}_{0.5}\text{Ca}_{0.5}\text{MnO}_3$ is paramagnetic at room temperature and changes on cooling to a mainly FM metallic phase at Curie temperature $T_C \approx 220$ K, and subsequently to charge-ordered antiferromagnetic (CO-AFM) phase at $T_{CO} \approx 150$ K (180 K upon warming)¹³⁵. The CE-state (combination of C-AFM and E-AFM type) is observed for $x = 0.5$ doping, which contains "zigzag" FM arrays of t_{2g} spins, coupled antiferromagnetically perpendicular to the zigzag direction⁹⁴(Fig. 4.2).

It has been established that this system is better described as magnetically phase-segregated over a wide range of temperatures^{136,137}, a phenomenon called phase separation (PS). At low temperatures, $T < T_{CO}$; FM metallic regions are trapped in a CO-AFM matrix and cannot grow against CO in the application of moderate magnetic field, whereas at an intermediate temperature range ($T_{CO} < T < T_C$), the FM phase coexists with insulating non-FM regions. The FM phase is partially confined but can grow against the insulating one while applying a low magnetic field¹³⁷.

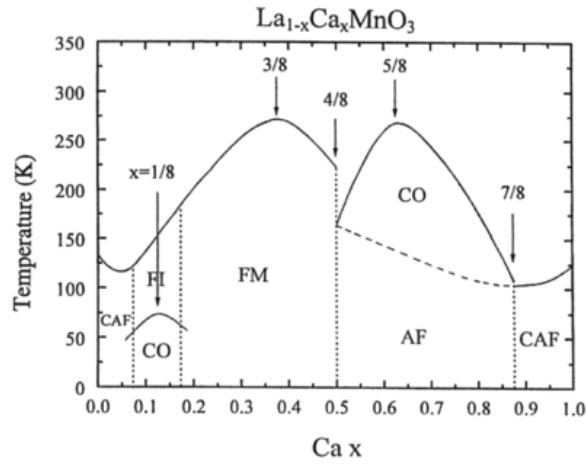


Fig. 4.1 Phase diagram of $\text{La}_{1-x}\text{Ca}_x\text{MnO}_3$, obtained using magnetization and resistivity data, reproduced from S.-W. Cheong and H. Y. Hwang. FM: ferromagnetic Metal, FI: Ferromagnetic Insulator, AF: Antiferromagnetism, CAF: Canted Antiferromagnetism and CO: Charge/Orbital Ordering. ^[88]

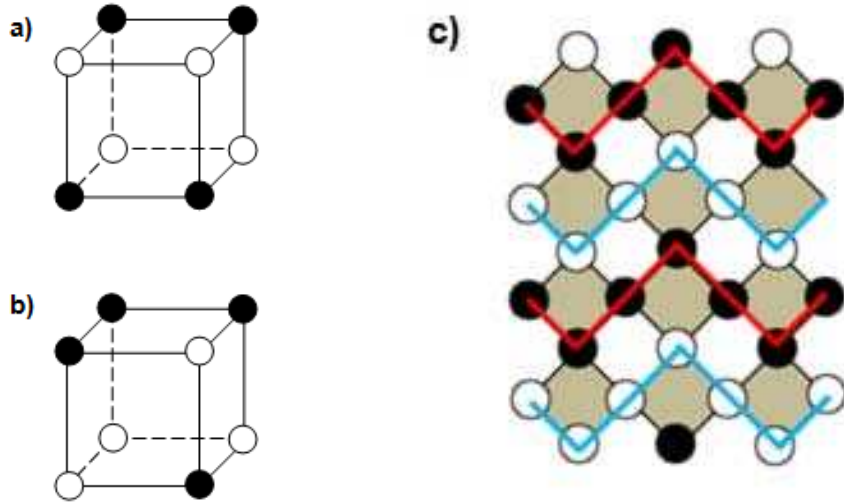


Fig. 4.2 a) C-type unit cell and b) E-type unit cell. c) The spin structure in plane at $x = 1/2$. Open can solid circle denote the spin up and down electrons, respectively. The white and gray squares denote the C- and E-type unit cells, respectively. At $x = 1/2$, C-type and E-type unit cells are equal. The thick blue and red lines indicate the zigzag FM path.

4.2 Samples and Experiments

At the STO/LSMO interface, a magnetic and electrical "dead" layer^{138,139} is presented due to the modifications at the interface, including stoichiometry, the presence of interfacial strain, and point defects such as oxygen vacancies. Thus, we insert a 1-nm thick $\text{La}_{0.5}\text{Ca}_{0.5}\text{MnO}_3$ layer at the STO/LSMO interface to avoid this effect.

The STO (200 nm)/ LCMO (1nm)/ LSMO (50 nm) oxide heterostructures were grown on STO (001) substrates by using a multi-target pulsed laser deposition system (KrF excimer laser 248 nm). The STO (200 nm)/LCMO (1 nm)/ LSMO (50 nm) epitaxial trilayer was deposited at a temperature of 750 °C in flowing oxygen of 300 mtorr and cooled down in the same oxygen pressure (oxygen poor condition). The indium-tin-oxide (ITO) (30 nm) layer was deposited in situ at 50 °C in 10 mtorr oxygen. The oxygen vacancy concentration of STO is reduced by in-situ annealing the sample in 600 mtorr O_2 at 450 °C for 0.5 hour, making it less n-type than the non-annealed one.

All optical experiments are performed at 80 K below the Curie temperature by placing the samples in a cryostat cooled by liquid nitrogen. MSHG is used to characterize the interfacial magnetic property and Magneto-Optical Kerr effect (MOKE) is performed to characterize the bulk magnetic property. To study the interfacial ME coupling effect, an external magnetic field is applied in plane, and an external electric field is applied out of the plane using a "Keithley 2400 Sourcemeter".

4.3 Results and discussion

4.3.1 Interfacial magnetic transition induced by magnetoelectric effect

A typical diode effect is displayed in oxygen-poor STO/LCMO/LSMO sample (Fig. 4.3), indicating a good n-type semiconductor is formed. The interfacial magnetic property is selectively probed with the method of magnetization-induced second-harmonic generation (MSHG). Figure 4.4 displays the voltage-dependent MSHG hysteresis loops in the range from -4 V to +4 V. The voltage-dependent magnetic contrast A is calculated and is shown in Fig. 4.5. When the gate voltage U_g is below -0.5 V, MSHG hysteresis loops are observed. They vanish at higher voltage. Again, the FM-AFM transition is observed with external electric field applied.

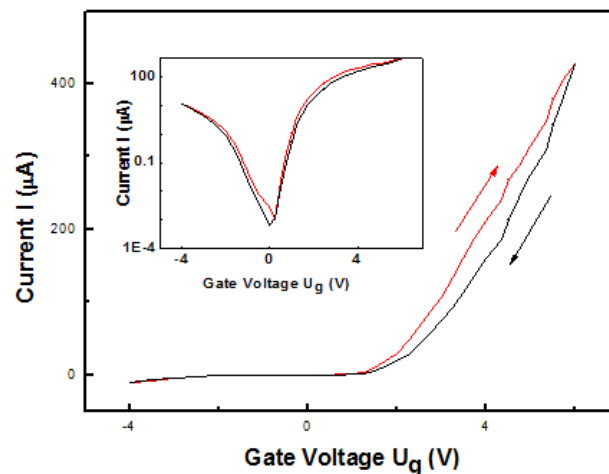


Fig. 4.3 Current-Voltage (I-V) curve shows diode effect. Inset is the semi-log curve.

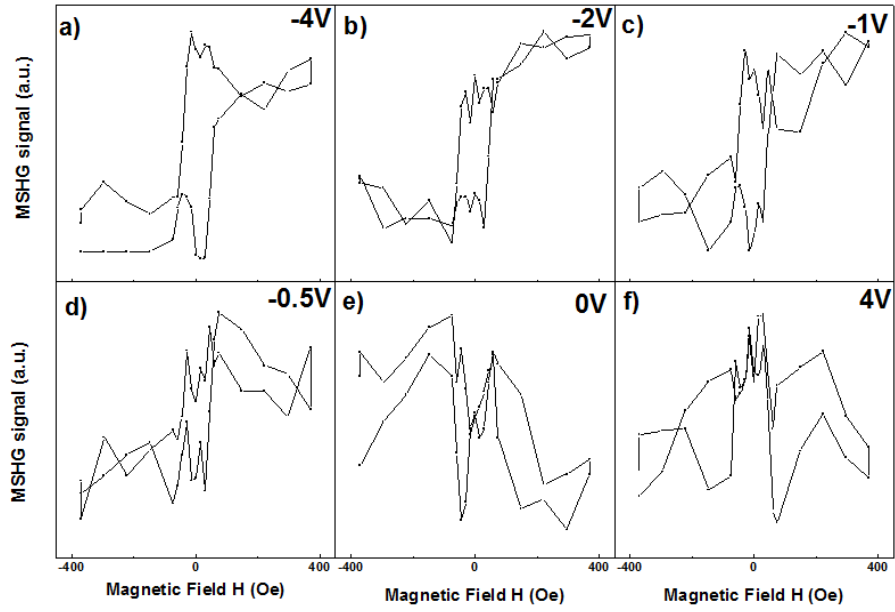


Fig. 4.4 MSHG hysteresis loops at different voltage.

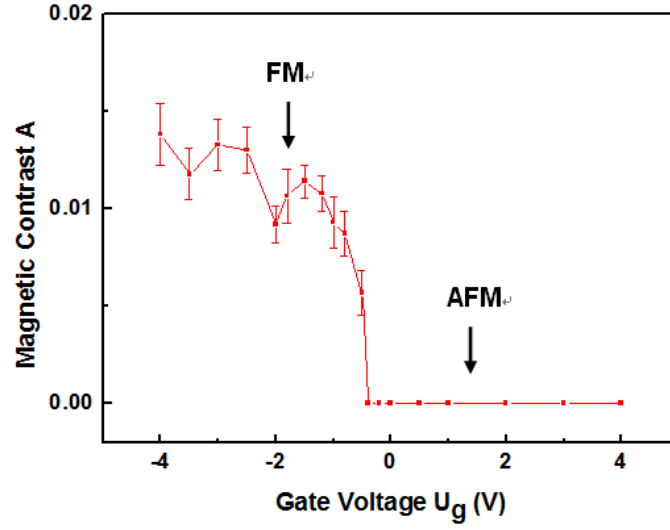


Fig. 4.5 Magnetic contrast A determined from MSHG measurements as a function of gate voltage U_g .

However, the magnetic transition happens at negative voltage around $U_c = -0.5$ V, which is different from BaTiO₃ (BTO)/LSMO samples, where it occurs at positive gate voltage. Some possible reasons may contribute to this:

i) The tensile strain due to the lattice mismatch between LSMO and STO would cause LSMO to be on the verge of an A-type AFM. This instability toward the AFM phase reduces the FM coupling in LSMO at the interface^{82,140}; ii) STO produces a dead layer in the adjacent LSMO, because the STO layer acts as a hole-donating layer. It has been considered that the valence-mismatched interface induces the charge transfer and that the overdoped LSMO is dominated by the AFM spin^{58,141,142}; iii) Ca may segregate to the surface of the growing epitaxial thin film, leading to a Ca rich LCMO layer at STO/LCMO interface¹⁴³, which pushes it further to the CO-AFM state. These effects would push the sample to an AFM state at zero applied electric field and no magnetic contrast is detected. When a negative voltage is applied, the electrons would accumulate at the interface and push the hole-doping level x to smaller value. Hence, the interfacial LSMO layer displays the FM configuration at -0.5 V.

MOKE experiments are also performed to detect the bulk property of LSMO. MOKE hysteresis loops are observed over the whole voltage range (Fig. 4.6). The MOKE contrast A is calculated and displayed in Fig. 4.7, which do not exhibit much change. Thus the ME coupling has no effect on the bulk magnetic property, and again constitutes an interfacial effect. Furthermore, voltage-dependent $P_{in}P_{out}$ and $S_{in}S'_{out}$ are measured. The voltage-dependent

$P_{in}P_{out}$ reveals a strong electric-field-induced SHG response (Fig. 4.8).

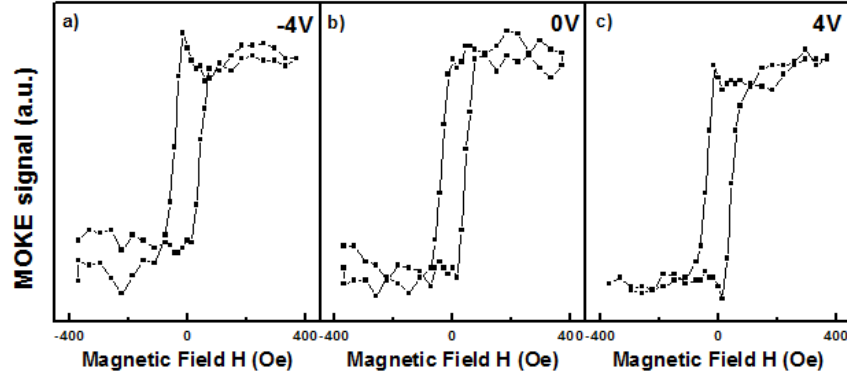


Fig. 4.6 MOKE hysteresis loops at different voltage.

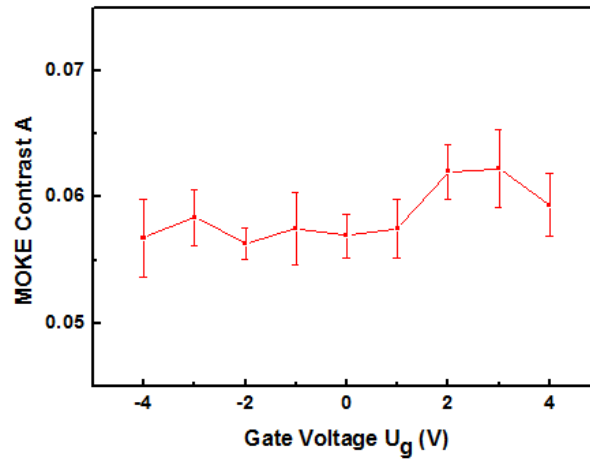


Fig. 4.7 MOKE contrast A as a function of gate voltage U_g .

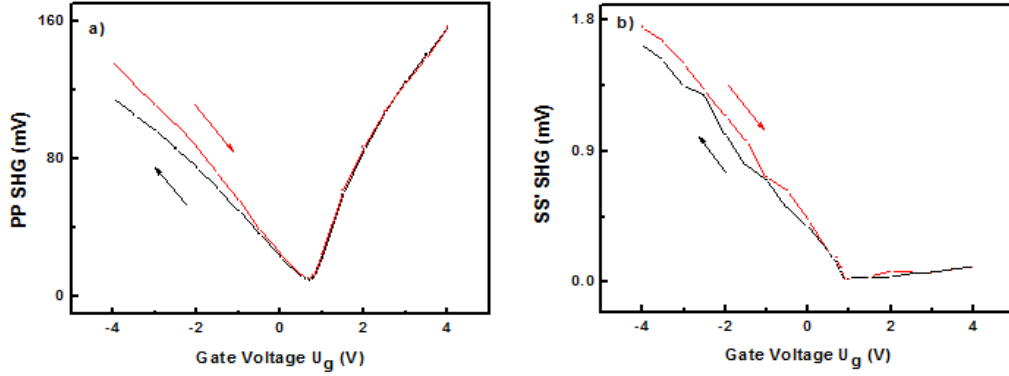


Fig. 4.8 a) $P_{in}P_{out}$ and b) $S_{in}S'_{out}$ SHG measured at 80K.

4.3.2 Effects of dopants in $SrTiO_3$

Oxygen-rich STO (200 nm)/LCMO (1nm)/ LSMO (50 nm) is fabricated for further study. Figure 4.9 displays the I-V curve exhibiting a diode effect with higher forward current than previous one. Figure 4.10 displays the MSHG loops measured at a series of voltage varying from -4 V to +4 V. The voltage-dependent magnetic contrast A is presented in Fig. 4.11. The FM-AFM transition is observed at -1 V prior to the transition of oxygen-poor sample ($U_c = -0.5$ V). This is attributed to the lower carrier (electron) concentration of STO. Thus, a larger negative voltage is required to push the interfacial LSMO layer to the doping level in favor of FM configuration. With small electric field applied, no loop is observed due to the formation of the complicated CE phase. Different from all previously studied samples, the hysteresis loop surprisingly

reappears at +2.5V. A possible explanation is that the hole doping level in the interfacial LSMO layer is far above 0.5 and an A-type AFM spin configuration is favored in this situation. In this state, FM order is favored in the LSMO intralayer and AFM coupling occurs perpendicular to the plane. Hence a magnetic hysteresis loop will be observed in the MSHG measurement. The lattice constant of STO, LSMO, BTO are 3.905Å, 3.871Å,¹⁴⁴ 3.992Å,¹¹⁴ respectively. Thus, the lattice mismatch is 0.87% between STO and LSMO, while it is 3.12% between BTO and LSMO. The stronger tensile strain in the plane would correspond to more compression perpendicular to the plane. Thus, the interlayer coupling in STO/LCMO/LSMO is weaker than for BTO. Hence, A-type AFM coupling maybe detected in STO/LCMO/LSMO sample, rather than in BTO/LCMO/LSMO sample. For comparison, MOKE hysteresis loops at different gate voltage U_g is displayed in Fig. 4.12, which reveals no modulation of bulk property.

Figure 4.13a) and b) present the voltage-dependent $P_{in}P_{out}$ and $S_{in}S'_{out}$ SHG measurements, respectively. The larger $S_{in}S'_{out}$ SHG signal at positive voltage as compared to oxygen-poor sample, may explain why the hysteresis loop does not reappear in oxygen-poor sample at high positive voltage.

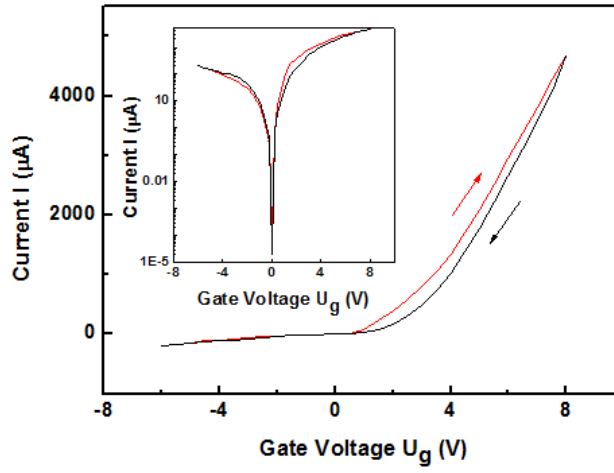


Fig. 4.9 Current-Voltage (I-V) curve shows diode effect. Inset is the semi-log curve.

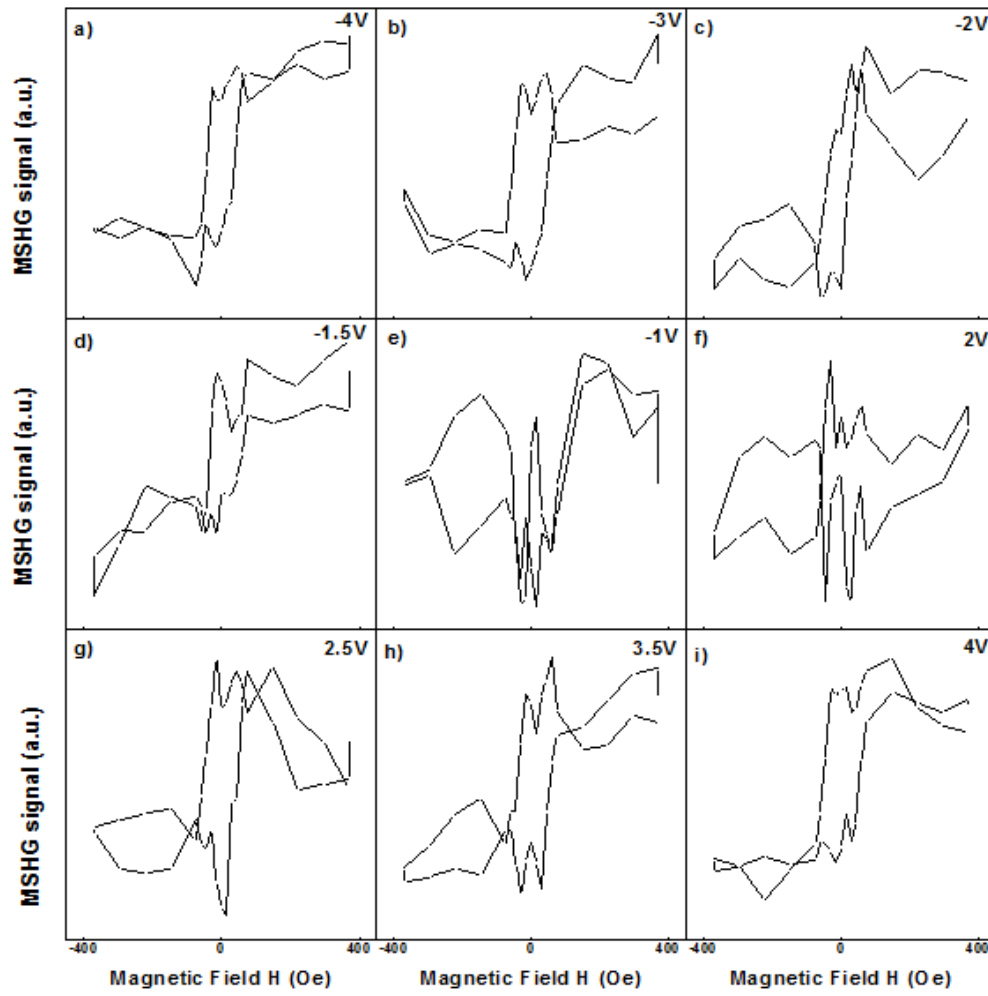


Fig. 4.10 MSHG hysteresis loops at different voltage.

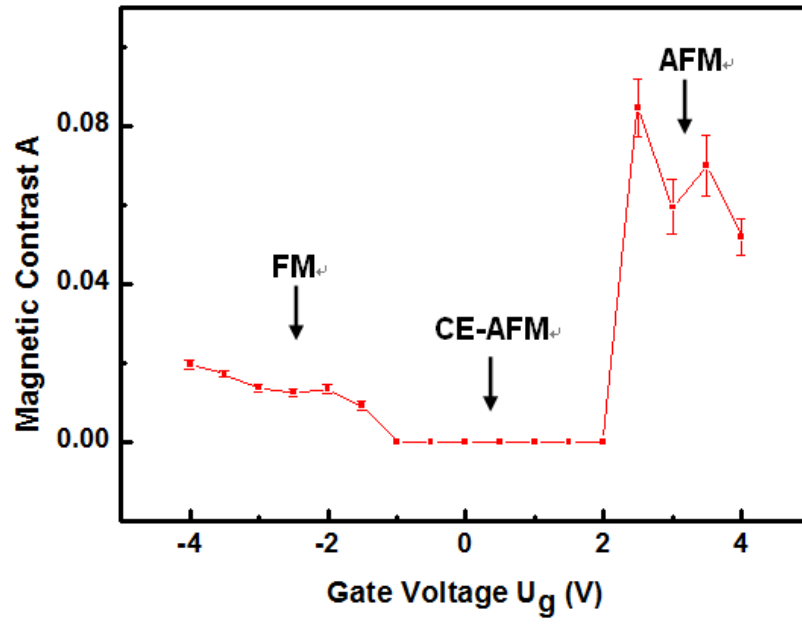


Fig. 4.11 MSHG magnetic contrast A as a function of gate voltage U_g .

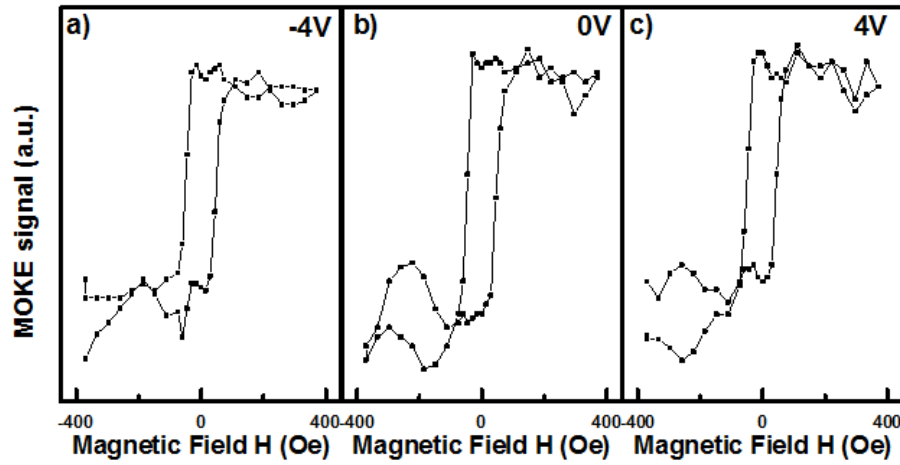


Fig. 4.12 MOKE hysteresis loops at different voltage.

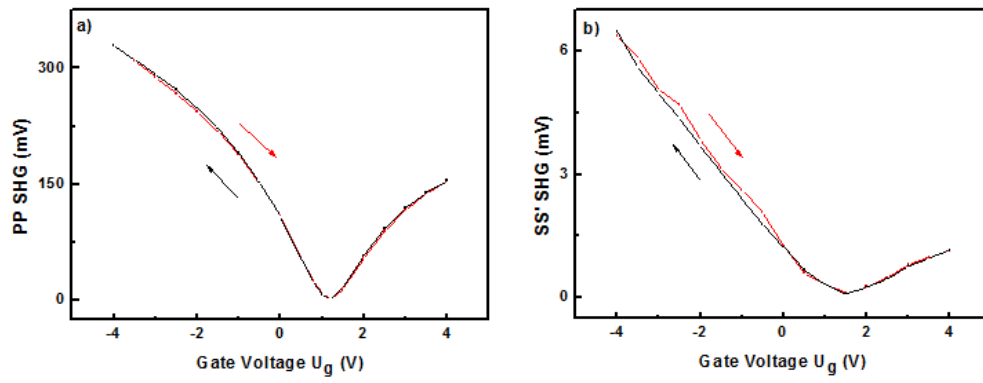


Fig. 4.13 a) $P_{in}P_{out}$ and b) $S_{in}S'_{out}$ SHG measured at 80K.

Chapter 5

Summary

Transition metal oxides (TMOs) have attracted much attention in recent years. The strong coupling between charge, spin, and orbital degrees of freedom creates novel functional properties. The research at the interplay between ferromagnetism, ferroelectricity and conductivity provides a promising way to the development of future spintronic devices.

The interface characterization of multifunctional oxide heterostructures is crucial to understand deeply the magnetic response, spin injection and spin transport. We characterize optically the magnetic property with the method of magnetization-induced second-harmonic generation (MSHG), which is a sensitive technique to selectively probe the interface where the spatial inversion symmetry is broken.

The interface of n-type BaTiO_3 (BTO)/ $\text{La}_{0.67}\text{Sr}_{0.33}\text{MnO}_3$ (LSMO) forms a Schottky barrier and displays a good diode effect. By applying an external electric field across the sample, we observe the magnetoelectric (ME) coupling effect to modulate the interface magnetization. The voltage dependent magnetic contrast sharply vanishes at positive voltage (applied to LSMO contact) and reveals a ferromagnetic (FM)-to- antiferromagnetic (AFM) transition occurring at the interface, while the magneto-optic Kerr effect (MOKE) indicates that the bulk property is not affected. The strain mediated

mechanism and ferroelectric (FE) polarization induced charge mediated mechanism are both discussed, but they do not play an important role in the observed magnetization transition. A new mechanism is proposed - the injected minority spins through strong Hund's interaction with the local magnetic moments at positive voltage weaken the double-exchange interaction of nearby Mn e_g electrons, thereby reducing the ferromagnetic (FM) ordering. The dominant superexchange interaction of localized t_{2g} electrons finally leads to the AFM configuration. By reducing the electron carrier concentration of BTO, a positive voltage shift of the transition is observed. The oxygen richer sample with lower carrier concentration requires a higher voltage to increase the hole doping level of LSMO to induce the interfacial AFM phase. By inserting a thin (1nm) $\text{La}_{0.5}\text{Ca}_{0.5}\text{MnO}_3$ layer between BTO and LSMO, the interface magnetic response from LSMO is enhanced.

Furthermore, a non-multiferroic heterostructure SrTiO_3 (STO)/ $\text{La}_{0.5}\text{Ca}_{0.5}\text{MnO}_3$ (LCMO)/ $\text{La}_{0.67}\text{Sr}_{0.33}\text{MnO}_3$ (LSMO) is studied. In this system, the interface FM-AFM transition is observed at negative voltage. The STO layer may act as a hole-donating layer, which induces the hole transfer to LSMO making it overdoped, while the LCMO interlayer at the 0.5 hole doping level displays complicated CE type AFM phase. Thus the AFM phase is dominant at the interface and electron accumulation is required to induce the FM phase by applying a negative voltage. For oxygen rich sample, the magnetic MSHG loop reappears at high positive voltage (around +2.5 V). At

high doping level ($x > 0.5$), LSMO exhibits A-type AFM order, consisting of AFM superexchange coupling between adjacent layers and intralayer FM double-exchange coupling. The less tensile strain of STO and LSMO due to a smaller lattice mismatch as compared to BTO would result in a weaker interlayer coupling. Thus, interfacial A-type AFM order can occur in STO/LCMO/LSMO heterostructure at high hole doping concentration.

The study of ME coupling of multifunctional oxide heterostructures is definitely important to the development and performance of future spintronic devices. The results presented here regarding the interfacial magnetic transition controlled by an external electric field offer some new perspective to study the spin transport of magnetic tunnel junctions.

Bibliography

1. Baibich, M. N. *et al.* Giant Magnetoresistance of (001)Fe/(001)Cr Magnetic Superlattices. *Phys. Rev. Lett.* 61, 2472–2475 (1988).
2. Chappert, C., Fert, A. & Van Dau, F. N. The emergence of spin electronics in data storage. *Nat. Mater.* 6, 813–823 (2007).
3. Wang, D. *et al.* 70% TMR at Room Temperature for SDT Sandwich Junctions With CoFeB as Free and Reference Layers. *IEEE Trans. Magn.* 40, 2269–2271 (2004).
4. Parkin, S. S. P. *et al.* Giant tunnelling magnetoresistance at room temperature with MgO (100) tunnel barriers. *Nat. Mater.* 3, 862–867 (2004).
5. Yuasa, S., Nagahama, T., Fukushima, A., Suzuki, Y. & Ando, K. Giant room-temperature magnetoresistance in single-crystal Fe/MgO/Fe magnetic tunnel junctions. *Nat. Mater.* 3, 868–871 (2004).
6. Lee, Y. M., Hayakawa, J., Ikeda, S., Matsukura, F. & Ohno, H. Effect of electrode composition on the tunnel magnetoresistance of pseudo-spin-valve magnetic tunnel junction with a MgO tunnel barrier. *Appl. Phys. Lett.* 90, 212507 (2007).
7. Daughton, J. M. Magnetic tunneling applied to memory (invited). *J. Appl. Phys.* 81, 3758 (1997).
8. Albert, F. J., Katine, J. A., Buhrman, R. A. & Ralph, D. C. Spin-polarized current switching of a Co thin film nanomagnet. *Appl. Phys. Lett.* 77, 3809 (2000).
9. Sun, J. Z. Spin-current interaction with a monodomain magnetic body: A model study. *Phys. Rev. B* 62, 570–578 (2000).

10. Zhang, S. Spin-Dependent Surface Screening in Ferromagnets and Magnetic Tunnel Junctions. *Phys. Rev. Lett.* 83, 640–643 (1999).
11. Duan, C.-G., Nan, C.-W., Jaswal, S. S. & Tsymbal, E. Y. Universality of the surface magnetoelectric effect in half-metals. *Phys. Rev. B* 79, (2009).
12. Duan, C.-G., Jaswal, S. S. & Tsymbal, E. Y. Predicted Magnetoelectric Effect in Fe / BaTiO₃ Multilayers: Ferroelectric Control of Magnetism. *Phys. Rev. Lett.* 97, (2006).
13. *Multifunctional oxide heterostructures*. (Oxford University Press, 2012).
14. Giovannetti, G., Kumar, S., Ortix, C., Capone, M. & van den Brink, J. Microscopic Origin of Large Negative Magnetoelectric Coupling in Sr^{1/2}Ba^{1/2}MnO₃. *Phys. Rev. Lett.* 109, (2012).
15. Rossell, M. D. *et al.* Atomic Structure of Highly Strained BiFeO₃ Thin Films. *Phys. Rev. Lett.* 108, (2012).
16. Matsuda, M. *et al.* Magnetic Dispersion and Anisotropy in Multiferroic BiFeO₃. *Phys. Rev. Lett.* 109, (2012).
17. Jeong, J. *et al.* Spin Wave Measurements over the Full Brillouin Zone of Multiferroic BiFeO₃. *Phys. Rev. Lett.* 108, (2012).
18. Bersuker, I. B. Pseudo Jahn-Teller Origin of Perovskite Multiferroics, Magnetic-Ferroelectric Crossover, and Magnetoelectric Effects: The d⁰ – d¹⁰ Problem. *Phys. Rev. Lett.* 108, (2012).
19. Spaldin, N. A. MATERIALS SCIENCE: The Renaissance of Magnetoelectric Multiferroics. *Science* 309, 391–392 (2005).

20. Ramesh, R. & Spaldin, N. A. Multiferroics: progress and prospects in thin films. *Nat. Mater.* 6, 21–29 (2007).
21. Scott, J. F. Room-temperature multiferroic magnetoelectrics. *NPG Asia Mater.* 5, e72 (2013).
22. Kitagawa, Y. *et al.* Low-field magnetoelectric effect at room temperature. *Nat. Mater.* 9, 797–802 (2010).
23. Wang, L. *et al.* Electric control of magnetism at room temperature. *Sci. Rep.* 2, (2012).
24. Sanchez, D. A. *et al.* Room-temperature single phase multiferroic magnetoelectrics: $\text{Pb}(\text{Fe}, \text{M})_x(\text{Zr}, \text{Ti})_{(1-x)}\text{O}_3$ [M = Ta, Nb]. *J. Appl. Phys.* 113, 074105 (2013).
25. Keeney, L. *et al.* Magnetic Field-Induced Ferroelectric Switching in Multiferroic Aurivillius Phase Thin Films at Room Temperature. *J. Am. Ceram. Soc.* 96, 2339–2357 (2013).
26. Evans, D. M. *et al.* Magnetic switching of ferroelectric domains at room temperature in multiferroic PZTFT. *Nat. Commun.* 4, 1534 (2013).
27. Gich, M. *et al.* Multiferroic Iron Oxide Thin Films at Room Temperature. *Adv. Mater.* 26, 4645–4652 (2014).
28. Thomasson, A. *et al.* Room temperature multiferroicity in $\text{Ga}_{0.6}\text{Fe}_{1.4}\text{O}_3\text{:Mg}$ thin films. *J. Appl. Phys.* 113, 214101 (2013).
29. Wang, W. *et al.* Room-Temperature Multiferroic Hexagonal LuFeO_3 Films. *Phys. Rev. Lett.* 110, (2013).

30. Fiebig, M. Revival of the magnetoelectric effect. *J. Phys. Appl. Phys.* 38, R123–R152 (2005).
31. Eerenstein, W., Mathur, N. D. & Scott, J. F. Multiferroic and magnetoelectric materials. *Nature* 442, 759–765 (2006).
32. Cheong, S.-W. & Mostovoy, M. Multiferroics: a magnetic twist for ferroelectricity. *Nat. Mater.* 6, 13–20 (2007).
33. Wu, S. M. *et al.* Reversible electric control of exchange bias in a multiferroic field-effect device. *Nat. Mater.* 9, 756–761 (2010).
34. Wu, S. M. *et al.* Full Electric Control of Exchange Bias. *Phys. Rev. Lett.* 110, (2013).
35. Eerenstein, W., Wiora, M., Prieto, J. L., Scott, J. F. & Mathur, N. D. Giant sharp and persistent converse magnetoelectric effects in multiferroic epitaxial heterostructures. *Nat. Mater.* 6, 348–351 (2007).
36. Wang, J. J. *et al.* Effect of strain on voltage-controlled magnetism in BiFeO₃-based heterostructures. *Sci. Rep.* 4, (2014).
37. Burton, J. D. & Tsymbal, E. Y. Prediction of electrically induced magnetic reconstruction at the manganite/ferroelectric interface. *Phys. Rev. B* 80, (2009).
38. Vaz, C. A. F. *et al.* Origin of the Magnetoelectric Coupling Effect in Pb (Zr 0.2 Ti 0.8) O₃ / La 0.8 Sr 0.2 MnO₃ Multiferroic Heterostructures. *Phys. Rev. Lett.* 104, (2010).
39. Heron, J. T. *et al.* Electric-Field-Induced Magnetization Reversal in a Ferromagnet-Multiferroic Heterostructure. *Phys. Rev. Lett.* 107, (2011).

40. Mannhart, J. & Schlom, D. G. Oxide interfaces--an opportunity for electronics. *Science* 327, 1607–1611 (2010).
41. Zubko, P., Gariglio, S., Gabay, M., Ghosez, P. & Triscone, J.-M. Interface Physics in Complex Oxide Heterostructures. *Annu. Rev. Condens. Matter Phys.* 2, 141–165 (2011).
42. Hwang, H. Y. *et al.* Emergent phenomena at oxide interfaces. *Nat. Mater.* 11, 103–113 (2012).
43. Chakhalian, J., Millis, A. J. & Rondinelli, J. Whither the oxide interface. *Nat. Mater.* 11, 92–94 (2012).
44. He, Q. *et al.* Magnetotransport at Domain Walls in BiFeO₃. *Phys. Rev. Lett.* 108, (2012).
45. Geng, Y. *et al.* Direct visualization of magnetoelectric domains. *Nat. Mater.* 13, 163–167 (2013).
46. Fechner, M. *et al.* Magnetic phase transition in two-phase multiferroics predicted from first principles. *Phys. Rev. B* 78, (2008).
47. Zhuravlev, M. Y., Sabirianov, R. F., Jaswal, S. S. & Tsymbal, E. Y. Giant Electroresistance in Ferroelectric Tunnel Junctions. *Phys. Rev. Lett.* 94, (2005).
48. Kohlstedt, H., Pertsev, N. A., Rodríguez Contreras, J. & Waser, R. Theoretical current-voltage characteristics of ferroelectric tunnel junctions. *Phys. Rev. B* 72, (2005).
49. Yin, Y. W. *et al.* Enhanced tunnelling electroresistance effect due to a ferroelectrically induced phase transition at a magnetic complex oxide interface. *Nat. Mater.* 12, 397–402 (2013).

50. Tsymbal, E. Y. APPLIED PHYSICS: Tunneling Across a Ferroelectric. *Science* 313, 181–183 (2006).
51. Wang, W.-G., Li, M., Hageman, S. & Chien, C. L. Electric-field-assisted switching in magnetic tunnel junctions. *Nat. Mater.* 11, 64–68 (2011).
52. Tsymbal, E. Y. Spintronics: Electric toggling of magnets. *Nat. Mater.* 11, 12–13 (2011).
53. Pantel, D., Goetze, S., Hesse, D. & Alexe, M. Reversible electrical switching of spin polarization in multiferroic tunnel junctions. *Nat. Mater.* 11, 289–293 (2012).
54. Ohtomo, A., Muller, D. A., Grazul, J. L. & Hwang, H. Y. Artificial charge-modulation in atomic-scale perovskite titanate superlattices. *Nature* 419, 378–380 (2002).
55. Okamoto, S. & Millis, A. J. Electronic reconstruction at an interface between a Mott insulator and a band insulator. *Nature* 428, 630–633 (2004).
56. Verbeeck, J., Lebedev, O. I., Van Tendeloo, G. & Mercey, B. SrTiO₃ (100) / (LaMnO₃)_m (SrMnO₃)_n layered heterostructures: A combined EELS and TEM study. *Phys. Rev. B* 66, (2002).
57. Pailloux, F. *et al.* Nanoscale analysis of a SrTiO₃ / La_{2/3}Sr_{1/3}MnO₃ interface. *Phys. Rev. B* 66, (2002).
58. Yamada, H. Engineered Interface of Magnetic Oxides. *Science* 305, 646–648 (2004).
59. Lüpke, G. Characterization of semiconductor interfaces by second-harmonic generation. *Surf. Sci. Rep.* 35, 75–161 (1999).

60. Shen, Y. R. *The principles of nonlinear optics*. (Wiley-Interscience, 2003).
61. LANDAU, L. D. & LIFSHITZ, E. M. *Electrodynamics of continuous media vol. 8*. (1960).
62. Qiu, Z. Q. & Bader, S. D. Surface magneto-optic Kerr effect. *Rev. Sci. Instrum.* 71, 1243 (2000).
63. Daboo, C. *et al.* Vectorial magnetometry with the magneto-optic Kerr effect applied to Co/Cu/Co trilayer structures. *Phys. Rev. B* 47, 11852–11859 (1993).
64. Rasing, T. Nonlinear magneto-optics. *J. Magn. Magn. Mater.* 175, 35–50 (1997).
65. Rasing, T. Nonlinear magneto-optical probing of magnetic interfaces. *Appl. Phys. B Lasers Opt.* 68, 477–484 (1999).
66. Pan, R.-P., Wei, H. D. & Shen, Y. R. Optical second-harmonic generation from magnetized surfaces. *Phys. Rev. B* 39, 1229–1234 (1989).
67. Burton, J. D. & Tsymbal, E. Y. Magnetoelectric interfaces and spin transport. *Philos. Trans. R. Soc. Math. Phys. Eng. Sci.* 370, 4840–4855 (2012).
68. Vaz, C. A. F., Walker, F. J., Ahn, C. H. & Ismail-Beigi, S. Intrinsic interfacial phenomena in manganite heterostructures. *J. Phys. Condens. Matter* 27, 123001 (2015).
69. Ohtomo, A. & Hwang, H. Y. A high-mobility electron gas at the LaAlO₃/SrTiO₃ heterointerface. *Nature* 427, 423–426 (2004).

70. Ueda, K. Ferromagnetism in LaFeO₃-LaCrO₃ Superlattices. *Science* 280, 1064–1066 (1998).
71. Chakhalian, J. *et al.* Orbital reconstruction and covalent bonding at an oxide interface. *Science* 318, 1114–1117 (2007).
72. Tokura, Y. & Hwang, H. Y. Condensed-matter physics: Complex oxides on fire. *Nat. Mater.* 7, 694–695 (2008).
73. Reyren, N. *et al.* Superconducting interfaces between insulating oxides. *Science* 317, 1196–1199 (2007).
74. Garcia, V. *et al.* Ferroelectric control of spin polarization. *Science* 327, 1106–1110 (2010).
75. Volger, J. Further experimental investigations on some ferromagnetic oxidic compounds of manganese with perovskite structure. *Physica* 20, 49–66 (1954).
76. Kusters, R. M., Singleton, J., Keen, D. A., McGreevy, R. & Hayes, W. Magnetoresistance measurements on the magnetic semiconductor Nd_{0.5}Pb_{0.5}MnO₃. *Phys. B Condens. Matter* 155, 362–365 (1989).
77. von Helmolt, R., Wecker, J., Holzapfel, B., Schultz, L. & Samwer, K. Giant negative magnetoresistance in perovskitelike La_{2/3}Ba_{1/3}MnO_x ferromagnetic films. *Phys. Rev. Lett.* 71, 2331–2333 (1993).
78. Chahara, K., Ohno, T., Kasai, M. & Kozono, Y. Magnetoresistance in magnetic manganese oxide with intrinsic antiferromagnetic spin structure. *Appl. Phys. Lett.* 63, 1990 (1993).
79. Ju, H. L., Kwon, C., Li, Q., Greene, R. L. & Venkatesan, T. Giant magnetoresistance in La_{1-x}Sr_xMnO₃ films near room temperature. *Appl. Phys. Lett.* 65, 2108 (1994).

80. Jin, S. *et al.* Thousandfold Change in Resistivity in Magnetoresistive La-Ca-Mn-O Films. *Science* 264, 413–415 (1994).
81. Xiong, G. C. *et al.* Giant magnetoresistive memory effect in Nd_{0.7}Sr_{0.3}MnO₃ films. *Appl. Phys. Lett.* 67, 3031 (1995).
82. Fang, Z., Solovyev, I. V. & Terakura, K. Phase Diagram of Tetragonal Manganites. *Phys. Rev. Lett.* 84, 3169–3172 (2000).
83. Molegraaf, H. J. A. *et al.* Magnetoelectric Effects in Complex Oxides with Competing Ground States. *Adv. Mater.* 21, 3470–3474 (2009).
84. Dong, S., Zhang, X., Yu, R., Liu, J.-M. & Dagotto, E. Microscopic model for the ferroelectric field effect in oxide heterostructures. *Phys. Rev. B* 84, (2011).
85. Burton, J. D. & Tsymbal, E. Y. Giant Tunneling Electroresistance Effect Driven by an Electrically Controlled Spin Valve at a Complex Oxide Interface. *Phys. Rev. Lett.* 106, (2011).
86. Urushibara, A. *et al.* Insulator-metal transition and giant magnetoresistance in La_{1-x}Sr_xMnO₃. *Phys. Rev. B* 51, 14103–14109 (1995).
87. Kajimoto, R., Yoshizawa, H., Tomioka, Y. & Tokura, Y. Stripe-type charge ordering in the metallic A-type antiferromagnet Pr_{0.5}Sr_{0.5}MnO₃. *Phys. Rev. B* 66, (2002).
88. *Colossal magnetoresistive oxides.* (Gordon and Breach Science Publishers, 2000).
89. Ōtsuka, J. Electrostatic Interaction of d^n Systems in Tetragonal Fields. *J. Phys. Soc. Jpn.* 21, 596–620 (1966).

90. Castellani, C., Natoli, C. R. & Ranninger, J. Metal-insulator transition in pure and Cr-doped V_2O_3 . *Phys. Rev. B* 18, 5001–5013 (1978).
91. Zener, C. Interaction between the d -Shells in the Transition Metals. II. Ferromagnetic Compounds of Manganese with Perovskite Structure. *Phys. Rev.* 82, 403–405 (1951).
92. Moreo, A. Phase Separation Scenario for Manganese Oxides and Related Materials. *Science* 283, 2034–2040 (1999).
93. Fujishiro, H., Ikebe, M. & Konno, Y. Phase Transition to Antiferromagnetic State in $La_{1-x}Sr_xMnO_3$ ($x \geq 0.5$). *J. Phys. Soc. Jpn.* 67, 1799–1800 (1998).
94. Dagotto, E. *Nanoscale phase separation and colossal magnetoresistance: the physics of manganites and related compounds*. (Springer, 2003).
95. de Groot, R. A., Mueller, F. M., Engen, P. G. van & Buschow, K. H. J. New Class of Materials: Half-Metallic Ferromagnets. *Phys. Rev. Lett.* 50, 2024–2027 (1983).
96. Okimoto, Y. *et al.* Anomalous Variation of Optical Spectra with Spin Polarization in Double-Exchange Ferromagnet: $La_{1-x}Sr_xMnO_3$. *Phys. Rev. Lett.* 75, 109–112 (1995).
97. Hwang, H. Y., Cheong, S.-W., Ong, N. P. & Batlogg, B. Spin-Polarized Intergrain Tunneling in $La_{2/3}Sr_{1/3}MnO_3$. *Phys. Rev. Lett.* 77, 2041–2044 (1996).
98. de Boer, P. K., van Leuken, H., de Groot, R. A., Rojo, T. & Barberis, G. E. Electronic structure of $La_{0.5}Ca_{0.5}MnO_3$. *Solid State Commun.* 102, 621–626 (1997).

99. Damjanovic, D. Ferroelectric, dielectric and piezoelectric properties of ferroelectric thin films and ceramics. *Rep. Prog. Phys.* 61, 1267–1324 (1998).
100. Iijima, K., Terashima, T., Yamamoto, K., Hirata, K. & Bando, Y. Preparation of ferroelectric BaTiO₃ thin films by activated reactive evaporation. *Appl. Phys. Lett.* 56, 527 (1990).
101. Vaudin, M. D. *et al.* Texturing and Dielectric Properties of Laser Deposited BaTiO₃ Thin Films Grown on Heated Substrates. *MRS Proc.* 243, (1991).
102. Kuwabara, M., Takahashi, S. & Kuroda, T. Preparation of ferroelectric BaTiO₃ thin films on polycrystalline BaPbO₃ substrates by sol-gel processing and their electrical properties. *Appl. Phys. Lett.* 62, 3372 (1993).
103. Shieh, J., Yeh, J. H., Shu, Y. C. & Yen, J. H. Hysteresis behaviors of barium titanate single crystals based on the operation of multiple 90° switching systems. *Mater. Sci. Eng. B* 161, 50–54 (2009).
104. Fukuda, Y. *et al.* Dielectric Properties of (Ba, Sr)TiO₃ Thin Films and their Correlation with Oxygen Vacancy Density. *Jpn. J. Appl. Phys.* 36, L1514–L1516 (1997).
105. Jona, F. & Shirane, G. *Ferroelectric crystals*. (Dover Publications, 1993).
106. Wada, S. *et al.* Enhanced Piezoelectric Property of Barium Titanate Single Crystals with Engineered Domain Configurations. *Jpn. J. Appl. Phys.* 38, 5505–5511 (1999).
107. Kim, E. *et al.* Second-Harmonic Generation of Single BaTiO₃ Nanoparticles down to 22 nm Diameter. *ACS Nano* 7, 5343–5349 (2013).

108. Yoo, H.-I., Chang, M.-W., Oh, T.-S., Lee, C.-E. & Becker, K. D. Electrocoloration and oxygen vacancy mobility of BaTiO₃. *J. Appl. Phys.* 102, 093701 (2007).
109. Yin, Y. W. *et al.* Enhanced tunnelling electroresistance effect due to a ferroelectrically induced phase transition at a magnetic complex oxide interface. *Nat. Mater.* 12, 397–402 (2013).
110. Vaz, C. A. F., Hoffman, J., Ahn, C. H. & Ramesh, R. Magnetoelectric Coupling Effects in Multiferroic Complex Oxide Composite Structures. *Adv. Mater.* 22, 2900–2918 (2010).
111. Vaz, C. A. F. Electric field control of magnetism in multiferroic heterostructures. *J. Phys. Condens. Matter* 24, 333201 (2012).
112. Fernandes Vaz, C. A. & Staub, U. Artificial multiferroic heterostructures. *J. Mater. Chem. C* 1, 6731 (2013).
113. Huang, X. & Dong, S. Ferroelectric control of magnetism and transport in oxide heterostructures. *Mod. Phys. Lett. B* 28, 1430010 (2014).
114. Tazaki, R., Fu, D., Itoh, M., Daimon, M. & Koshihara, S. Lattice distortion under an electric field in BaTiO₃ piezoelectric single crystal. *J. Phys. Condens. Matter* 21, 215903 (2009).
115. Burton, J. D. & Tsymbal, E. Y. Evolution of the band alignment at polar oxide interfaces. *Phys. Rev. B* 82, (2010).
116. Ma, X. *et al.* Charge control of antiferromagnetism at PbZr_{0.52}Ti_{0.48}O₃/La_{0.67}Sr_{0.33}MnO₃ interface. *Appl. Phys. Lett.* 104, 132905 (2014).

117. Goren, D., Amir, N. & Nemirovsky, Y. Determination of the interface charge between an epilayer and a substrate using capacitance-voltage measurements. *J. Appl. Phys.* 71, 318 (1992).
118. Goren, D. & Nemirovsky, Y. Determination of interface properties between a depleted heteroepitaxial layer and a substrate from capacitance measurements. *J. Appl. Phys.* 77, 244 (1995).
119. Pintilie, L. & Alexe, M. Metal-ferroelectric-metal heterostructures with Schottky contacts. I. Influence of the ferroelectric properties. *J. Appl. Phys.* 98, 124103 (2005).
120. Pintilie, L. *et al.* Metal-ferroelectric-metal structures with Schottky contacts. II. Analysis of the experimental current-voltage and capacitance-voltage characteristics of $\text{Pb}(\text{Zr,Ti})\text{O}_3$ thin films. *J. Appl. Phys.* 98, 124104 (2005).
121. Bowen, M. *et al.* Nearly total spin polarization in $\text{La}_{2/3}\text{Sr}_{1/3}\text{MnO}_3$ from tunneling experiments. *Appl. Phys. Lett.* 82, 233 (2003).
122. Rana, K. G. *et al.* Hot electron transport in a strongly correlated transition-metal oxide. *Sci. Rep.* 3, (2013).
123. Neville, R. C. Permittivity of Strontium Titanate. *J. Appl. Phys.* 43, 2124 (1972).
124. Tomio, T., Miki, H., Tabata, H., Kawai, T. & Kawai, S. Control of electrical conductivity in laser deposited SrTiO_3 thin films with Nb doping. *J. Appl. Phys.* 76, 5886 (1994).
125. Guo, X. ., Chen, X. . & Lu, W. Optical properties of Nb doped SrTiO_3 from first principles study. *Solid State Commun.* 126, 441–446 (2003).

126. Lytle, F. W. X-Ray Diffractometry of Low-Temperature Phase Transformations in Strontium Titanate. *J. Appl. Phys.* 35, 2212 (1964).
127. Yamada, H. & Miller, G. R. Point defects in reduced strontium titanate. *J. Solid State Chem.* 6, 169–177 (1973).
128. Balachandran, U. & Eror, N. G. Electrical conductivity in strontium titanate. *J. Solid State Chem.* 39, 351–359 (1981).
129. Frederikse, H. P. R., Thurber, W. R. & Hosler, W. R. Electronic Transport in Strontium Titanate. *Phys. Rev.* 134, A442–A445 (1964).
130. Tufte, O. N. & Chapman, P. W. Electron Mobility in Semiconducting Strontium Titanate. *Phys. Rev.* 155, 796–802 (1967).
131. Vigliante, A. *et al.* Coupling between lattice distortions and magnetism in $\text{La}_{0.9}\text{Sr}_{0.1}\text{MnO}_3$ thin films. *Europhys. Lett. EPL* 54, 619–625 (2001).
132. Bellingeri, E., Pellegrino, L., Marré, D., Pallecchi, I. & Siri, A. S. All-SrTiO₃ field effect devices made by anodic oxidation of epitaxial semiconducting thin films. *J. Appl. Phys.* 94, 5976 (2003).
133. Zhou, Q. *et al.* Transport property in SrTiO₃ *p* - *n* junction. *Europhys. Lett. EPL* 71, 283–289 (2005).
134. Zhu, S. *et al.* Coexistence of large positive and negative magnetoresistance in $\text{La}_{0.7}\text{Ca}_{0.3}\text{MnO}_3$ films with microcracks. *J. Magn. Magn. Mater.* 313, 361–365 (2007).
135. Schiffer, P., Ramirez, A. P., Bao, W. & Cheong, S.-W. Low Temperature Magnetoresistance and the Magnetic Phase Diagram of $\text{La}_{1-x}\text{Ca}_x\text{MnO}_3$. *Phys. Rev. Lett.* 75, 3336–3339 (1995).

136. Levy, P. *et al.* Controlled phase separation in $\text{La}_{0.5}\text{Ca}_{0.5}\text{MnO}_3$. *Phys. Rev. B* 62, 6437–6441 (2000).
137. Freitas, R. S., Ghivelder, L., Levy, P. & Parisi, F. Magnetization studies of phase separation in $\text{La}_{0.5}\text{Ca}_{0.5}\text{MnO}_3$. *Phys. Rev. B* 65, (2002).
138. Huijben, M. *et al.* Critical thickness and orbital ordering in ultrathin $\text{La}_{0.7}\text{Sr}_{0.3}\text{MnO}_3$ films. *Phys. Rev. B* 78, (2008).
139. Herger, R. *et al.* Structure determination of monolayer-by-monolayer grown $\text{La}_{1-x}\text{Sr}_x\text{MnO}_3$ thin films and the onset of magnetoresistance. *Phys. Rev. B* 77, (2008).
140. Konishi, Y. *et al.* Orbital-State-Mediated Phase-Control of Manganites. *J. Phys. Soc. Jpn.* 68, 3790–3793 (1999).
141. Izumi, M. *et al.* Insulator-metal transition induced by interlayer coupling in $\text{La}_{0.6}\text{Sr}_{0.4}\text{MnO}_3 / \text{SrTiO}_3$ superlattices. *Phys. Rev. B* 64, (2001).
142. Ogimoto, Y. *et al.* Tunneling Magnetoresistance above Room Temperature in $\text{La}_{0.7}\text{Sr}_{0.3}\text{MnO}_3 / \text{SrTiO}_3 / \text{La}_{0.7}\text{Sr}_{0.3}\text{MnO}_3$ Junctions. *Jpn. J. Appl. Phys.* 42, L369–L372 (2003).
143. Simon, J. *et al.* Diffusion and segregation effects in doped manganite/titanate heterostructures. *Appl. Phys. Lett.* 84, 3882 (2004).
144. Belenky, L. J., Ke, X., Rzchowski, M. & Eom, C. B. Epitaxial $\text{La}_{0.67}\text{Sr}_{0.33}\text{MnO}_3 / \text{La}_{0.67}\text{Ba}_{0.33}\text{MnO}_3$ superlattices. *J. Appl. Phys.* 97, 10J107 (2005).